2021

Nonlinear Light-matter Interactions in Novel Crystals for Broadband Mid-infrared Generation

Taiki Kawamori
University of Central Florida

NONLINEAR LIGHT-MATTER INTERACTIONS IN NOVEL CRYSTALS FOR BROADBAND MID-INFRARED GENERATION

by

TAIKI KAWAMORI

B.S. Keio University, 2016

M.S. University of Central Florida, 2019

A dissertation submitted in partial fulfillment of the requirements
for the degree of Doctor of Philosophy
in CREOL, the College of Optics and Photonics
at the University of Central Florida
Orlando, Florida

Fall Term

2021

Major Professor: Konstantin L. Vodopyanov

ABSTRACT

Mid-infrared (MIR) laser sources have demonstrated diverse applications in science and technology. For spectroscopy applications, numerous molecules have unique absorption features in this range, and one needs a spectrally broad coherent laser source for parallel detection of mixtures of species. Frequency down-conversion in nonlinear optical materials via second-order nonlinear susceptibility is one of the promising techniques to generate the spectral coverage of more than an octave in the MIR, assisted by emerging novel crystals. The nonlinear light-matter interactions in such special crystals as ZnSe ceramics have not been analyzed. Additionally, through the use of high-intensity few-cycle optical pulses, high-order nonlinear effects such as four-wave mixing, multiphoton absorption, and nonlinear refraction come into play beyond conventional second-order nonlinear interaction. In this thesis, the nonlinear interactions for generating broadband MIR were studied through both experimental and numerical approaches. First, a nonlinear frequency conversion model based on random phase matching was developed in zinc-blende polycrystalline structures. Monte Carlo simulation statistically verifies that a disordered material could perform on par with a quasi-phase-matched material for frequency conversion in ultrafast interactions. Second, the nonlinear interaction in orientation-patterned GaP combined with an optical parametric oscillator was numerically analyzed. A wave propagation model discovers that third-order nonlinearity plays an important role in the process of spectral evolution. Finally, using a 2.35-μm Cr:ZnS mode-locked laser, nonlinear absorption and nonlinear refractive index were characterized in the Z-scan technique for GaP, ZnSe, GaSe, and ZGP crystals. The visualization of nonlinear interactions and the uncovering of nonlinear parameters will be a

guide for optimizing experimental systems and will further advance the development of MIR laser sources.

ACKNOWLEDGMENTS

I would like to express my deepest appreciation to my advisor, Dr. Konstantin L. Vodopyanov for his invaluable guidance and support. The discussions I had with him on various issues and his approach to science had a great positive impact on my research life. It has been a great honor and pleasure working with him. I would also like to thank the members of my dissertation committee, Dr. Aristide Dogariu, Dr. Sasan Fathpour, and Dr. Robert Peale, for reviewing the manuscript and their insightful comments, which led me to have a wide perspective of my research. Many thanks to my lab mates in the MIR Combs lab, Dr. Qitian Ru, Dr. Andrey Muraviev, Dr. Ozarfar Gafarov, Dmitrii Konnov, Dr. Xuan Chen, and Dr. Zachary Loparo for constructive suggestions for the research and stimulus discussions on every topic. Especially, I learned much hands-on experimental skills with them. Special thanks to Dr. Sergey Vasilyev for practical discussion of a laser and to Dr. Peter Schunemann for providing novel crystals. I also gratefully acknowledge the assistance from CREOL staff members from my arrival to exit. Without all their efforts, I would not be able to complete my doctoral study. Last but not least, I would like to thank my parents for their unconditional support.

TABLE OF CONTENTS

LIST OF FIGURES

LIST OF TABLES

CHAPTER ONE: INTRODUCTION

Mid-Infrared Region

Many molecules have unique absorption features in the mid-infrared (MIR) region (2-20 μm in wavelengths). They have specific vibrational or rotational energy which is quantized to be resolved using coherent MIR lasers. As your smartphone identifies you using your fingerprint, you can identify the quantity of molecules based on pressure or temperature. MIR spectroscopy provides rich and quantitative information on the structure of matter for example with the technique of frequency comb spectroscopy. Optical frequency combs in the MIR region are powerful photonic tools that can be used in the most advanced spectroscopic techniques [1,2]. Such applications include dual combs spectroscopy, remote sensing, breath analysis, and combustion diagnostic.

Mid-Infrared Laser Sources

Various approaches have been developed in the last decade to generate MIR laser that includes mode-locked lasers [3], difference frequency generators (DFG) [4–6], intra-pulse DFG (IDFG) [7–10], tunable optical parametric oscillators (OPOs) [11,12], subharmonic OPOs [13–15], supercontinuum (SC) generator in fibers and waveguides [16,17], quantum cascade lasers [18], and micro-resonators. For spectroscopic detection of a mixture of multiple species, e.g. in the study of the dynamics of chemical reactions in combustion processes or in breath analysis, one needs a spectrally broad comb with enough power to achieve reasonable signal-to-noise ratio. Yet, fulfilling these metrics simultaneously has been challenging. Figure 1 shows the spectral coverage diagram for different methods. Note that here the time coherence properties are neglected. Each

method has advantages and disadvantages. For example, mode-locked lasers can have direct access to the MIR, however, the spectral coverage is limited up to the wavelength of 3 μm. IDFG and micro-resonators can suffer from either low conversion efficiency or low output power. The tunable OPO, DFG, and QCL have relatively narrow frequency span. SC can have strongly uneven spectral density distribution.

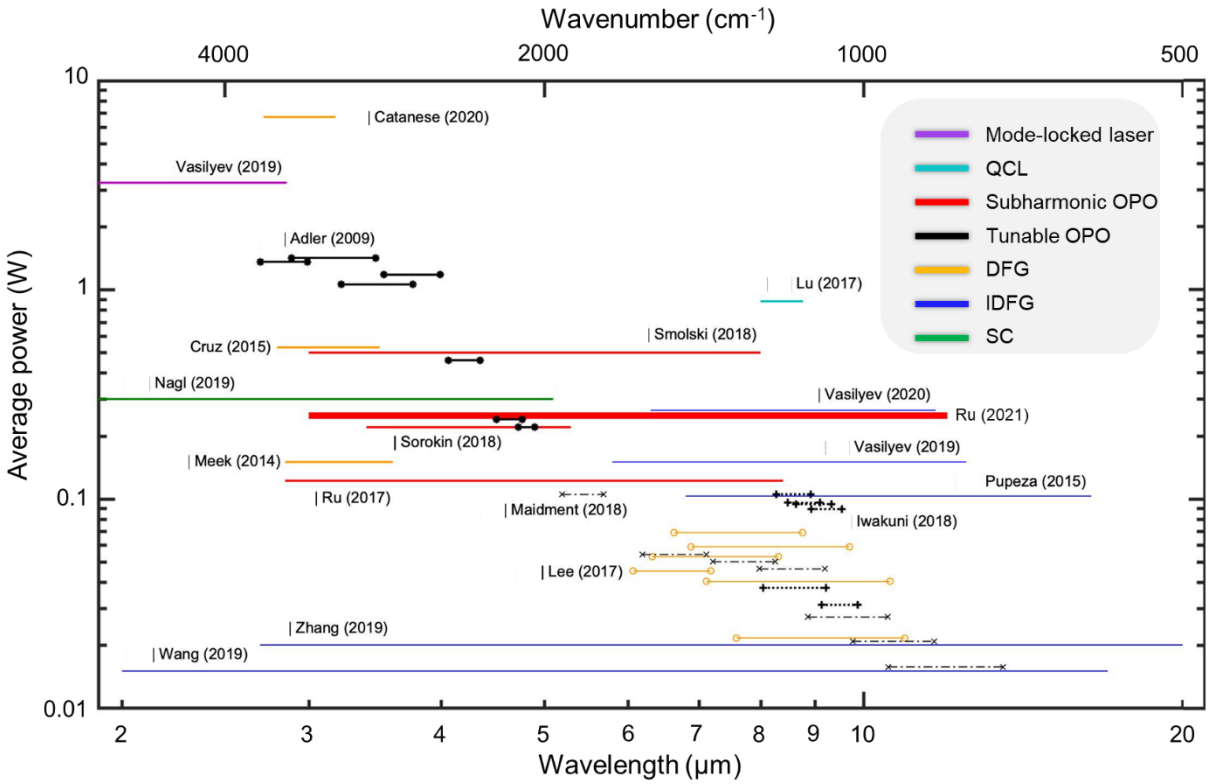

Figure 1. Frequency span and average power of selected frequency comb sources across the MIR.

Nonlinear Optical Materials in the Mid-Infrared

Nonlinear optical (NLO) materials have been widely used to convert laser wavelength to the wavelength that is technically hard to be produced. Recently, NLO materials (such as Lithium Niobate, GaAs, GaP, ZnSe, ZnS, GaSe, and ZGP) used as second-order nonlinearity get attentions because due to the increase in available laser power for the MIR generation, the third order nonlinearity comes to play a role with conventional second-order nonlinear effect. Therefore, the characterization of third-order nonlinear coefficient in this range is particularly important as it may negatively or positively affect to a system. For example, the spectrum can become broad due to self-phase modulation (SPM) and the change of refractive index can spatially produce the lens effect in nonlinear medium, leading to have self-focusing and -defocusing. In a phase-mismatched condition, where multi-step or cascaded quadratic nonlinearities come into play, the effective nonlinear refractive index needs to be addressed, which is a sum of the intrinsic Kerr nonlinearity and a term from cascaded quadratic mixing. In ultrafast OPO applications, only few papers report these phenomena.

Nonlinear Refractive Index

Nonlinear refractive index n_2 is a critical parameter for the phase shift and optical damage, especially in high-power laser system. In the wavelengths of interest for signal processing and communications, there have been a large number of studies on materials for using a large Kerr nonlinearity. There have been relatively few efforts for nonlinear material characterization in the MIR, but recently it is getting active research area thanks to the available laser sources [19–21]. In

the spectral region of 9-10 μm, for example, the maximum peak power in CO_2 laser demonstrated is 15 TW in a train of 3 ps pulses [22]. For better manipulation of this kind of laser beam and for achieving sub-picosecond long-wave-infrared pulse in a compressor, the suitable material needs to be addressed. Using CO_2 laser pulses, the nonlinear refractive index is deduced by measuring the four-wave mixing (FWM) efficiency [23]. They estimate the n_2 of ZnSe, GaSe, and $AgGaSe_2$ by comparing the experimental data with the well-known material GaAs in this range. GaP is another promising nonlinear crystal for its relatively large second-order nonlinear coefficient, a wide transparency range from visible to the mid-infrared (0.55-13 μm), and large direct bandgap of 2.79 eV. Its high nonlinear refractive index can be used combined with second-order nonlinearity in SC generation [24]. Also, orientation-patterned- (OP-) GaP was used for IDFG to produce an octave-wide frequency comb for spectroscopy applications [25]. The value of nonlinear refractive index n_2 in GaP has been reported in the rage of 1-1.75 μm [21,26–28]. However, no prior research measures the value at the MIR for GaP. Polycrystalline ZnSe emerges as an attractive quadratic nonlinear crystal for ultrafast OPO [29] and as a host for mid-infrared transition metal lasers [30]. The n_2 for ZnSe is measured at selected wavelength [20,31].

Nonlinear absorption

Recently, nonlinear absorption was observed in OP-GaP irradiated by a 2.35 μm Cr:ZnS laser [15]. The absorption was only a few percent, and it was small compared to the one of OP-GaAs, however, more detailed study must be done to determine its effect for further higher power laser system. No research has been conducted for 5-photon or 6-photon absorption in this crystal

but there is some research on 2PA, 3PA, and 4PA in different wavelengths. 2PA coefficient is measured to be 1.02 cm/GW using 800 nm pump pulse. 3PA coefficient is measured to be 0.14 cm^3/GW^2 at the polarization along [1 1 1] direction [26]. Recently, 4-photon absorption is also reported in GaP at 1.75 μm with the peak intensity up to 500 GW/cm^2 [21].

Random Phase-Matching

Random phase-matching (RPM) was first recognized in 1966 [32]. It has been used for specific nonlinear applications thanks the materials' broad acceptance bandwidth for frequency conversion. The developed theories appeared in 2004, and it was experimentally demonstrated [33]. Recently, using femtosecond laser pulses, broadband spectrum output in the MIR in the form of frequency down-conversion and supercontinuum generation was reported [29,34]. Also, RPM is used to produce high-harmonic generation [35]. Figure 2 shows the world's first randomly phase-matched OPO, producing the spectrum spanning 3 to 7.5 μm.

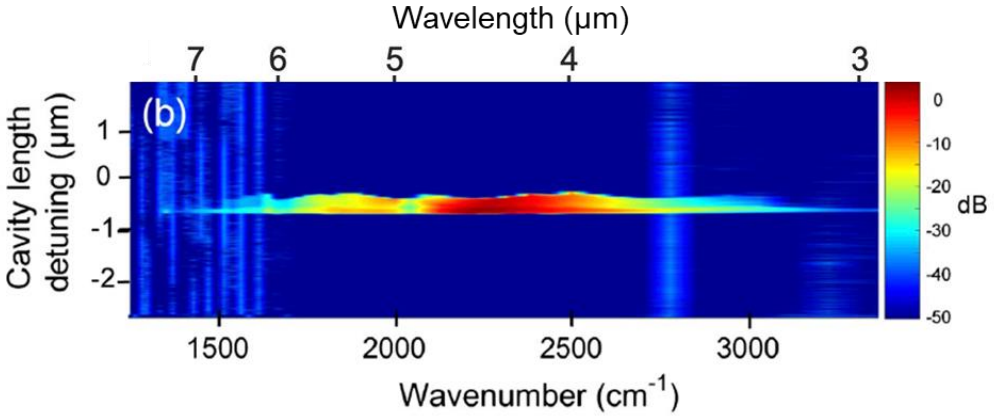

Figure 2. MIR output spectrum via randomly phase matched OPO [29].

RPM is an analogy of random walk, where the travel distance from the origin is proportional to the length of step and square root of the number of steps. After a number of steps, the person is no longer near the origin even though the process is random. In the context of interaction with nonlinear materials, the growth of generated electric field is not averaged to zero but has some magnitudes. Adding *E*-field generated from each mono-structure, the intensity grows linearly with the number of mono-structures. This process can happen in disordered materials for example in polycrystalline materials and crystalline powders. In the early stage of laser development, by changing the parameters of powder-layer thickness, average particle size, and laser beam diameter, the second-harmonic generation (SHG) in powders yielded the information to determine the magnitude of nonlinear optical coefficient. The feature of RPM was described in the powder technique for evaluating nonlinear optical materials [36] as follows. (i) The highest conversion is when the particle size is close to the coherence length. (ii) Conversion efficiency in intensity grows linearly with a sample thickness. (iii) At a fixed sample length and optimized conditions, the conversion efficiency is higher for larger coherence length. Therefore, RPM efficiency is somewhere between QPM and not phase-matched case, but not just zero.

Scope and Organization of Dissertation

This work aims to reveal the unique nonlinear interactions for the MIR generations and explore the possibilities for producing super-octave wide MIR spectrum. Chapter 2 describes the overview of nonlinear optics, specifically focus on second- and third-order nonlinear effects. Chapter 3 describes the modeling of frequency conversion in polycrystalline materials. Second-

order nonlinear interactions in disordered materials based on RPM suggest intriguing opportunities for extremely broadband frequency conversion. We present a quantitative realistic model for RPM in zinc-blende polycrystals that takes into account effects of random crystal orientation and grain-size fluctuations and includes polarization analysis of the generated output. Chapter 4 describes the simulation of pulse propagation in an optical parametric oscillator. We developed a theoretical model that provides an insight into new approach for generating multi-octave optical frequency combs. Theoretical analysis and numerical calculations show that the parametric process due to cubic nonlinearity importantly contributes to broadening the spectrum. Chapter 5 describes the experimental results for the nonlinear properties of samples such as GaP, ZnSe, GaSe, and ZGP. The measurements for nonlinear properties of absorption and refraction have been conducted to characterize the materials for the applications in the MIR. Chapter 6 summarizes the work in this thesis and outlook is described.

CHAPTER TWO: THEORY

Here, the theory of nonlinear optics will be explained, featuring second- and third-order nonlinear effects. When observing the light-matter interaction in high intensity field, the bonded electron to atom can oscillate with the higher frequency than the incoming *E*-field. The nonlinear induced polarization is expressed as

$$P(\omega) = \epsilon_0 \chi^{(1)} E(\omega) + \epsilon_0 \chi^{(2)} E^2(\omega) + \epsilon_0 \chi^{(3)} E^3(\omega) + \cdots \quad (1)$$

where ϵ_0 is the permittivity in vacuum, $\chi^{(n)}$ is n^{th} order susceptibility, and $E(\omega)$ is the electric field in the frequency domain [37].

Second-Order Nonlinear Optical Processes

Second-order nonlinear process through $\chi^{(2)}$ media includes second-harmonic generation (SHG), sum-frequency generation (SFG), difference frequency generation (DFG), and so on. Three photons are involved in the process for generating other frequency components while maintaining the energy and momentum conservation. Optical parametric generation (OPG) is another second-order process, where with one input of a beam both signal and idler waves are generated from quantum noise. Combining with the resonator, which is called an optical parametric oscillator (OPO), the wavelength can tune by crystal angle, temperature, or poling period.

Quasi Phase-Matching

Phase-matching is a critical factor for efficient frequency conversion. When the phase of the fundamental and the generated signal is not matched, the signal power oscillates periodically from zero to a certain power as it propagates inside media due to destructive interference. Birefringent crystals can have different refractive index for ordinary wave and extraordinary wave, leading for fundamental and signal waves to propagate at the same speed to avoid the destructive interference. When fundamental beam and generated beam, SHG in this case, propagate at the same speed, the efficiency increases quadratically with sample length.

Another way to compensate for the phase mismatch is to use quasi phase matched (QPM) materials. It was first proposed by Armstrong in 1962 [38]. QPM material is an engineered material, where the crystalline orientation is flipped for every coherence length. The coherence length is expressed as $L_c = \pi/\Delta k$, where Δk is the phase mismatch. Figure 3 shows the field growth of SHG in propagation distance for the phase-matched, QPM, and non-phase-matched case, showing that by flipping the sign of nonlinear coefficient, QPM signal grows quadratically. One of the most used materials is periodically poled lithium niobate (PPLN). For the MIR application PPLN has a limited transparency range up to 5 μm. The extensive study of fabricating orientation-patterned (OP-) GaAs and GaP has been done in the past decade to use QPM technique in the MIR region. Both OP-GaAs and OP-GaP have shown promising results for the MIR applications.

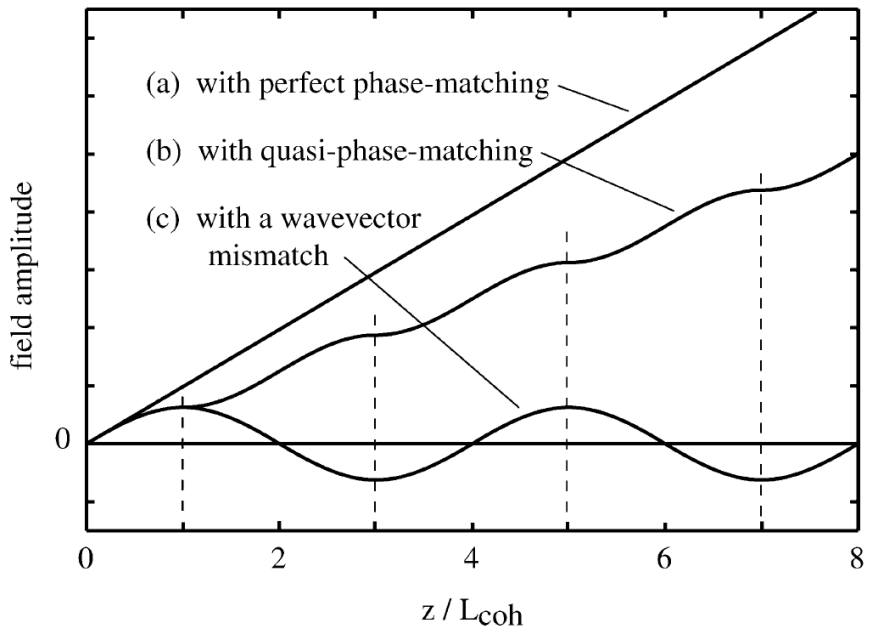

Figure 3. Diagram of conversion efficiency for using different methods: birefringent and quasi-phase-matched method [37].

Polarization-Dependent Frequency Conversion

The three-wave mixing in $\chi^{(2)}$ media is characterized by the second order of nonlinear polarization. $\chi^{(2)}$ is a second-order nonlinear susceptibility, which is a third-rank tensor having 27 components. The indices *ijk* in 3x3x3 matrix form refer to the polarization components of interacting fields. It can also be represented as 3x6 matrix as d_{jk}. For the zinc-blende crystal structure the formula is reduced, indicating that two orthogonal polarizations are needed to induce a polarization to the direction of principal axis in the crystal. This high symmetry of second-order susceptibility offers various nontrivial possibilities for nonlinear interactions between three waves,

with respect to their polarizations. The polarization dependence of three-wave mixing process in QPM GaAs has been explored in several experiments for several key crystallographic directions (Figure 4). When all three polarizations are parallel to [111] (the direction of the Ga-As bond, 35.3º with respect to [110]), the nonlinear coefficient is maximized. When a pump beam is polarized to [110], the output signal only has the polarization that is orthogonal to the input [39].

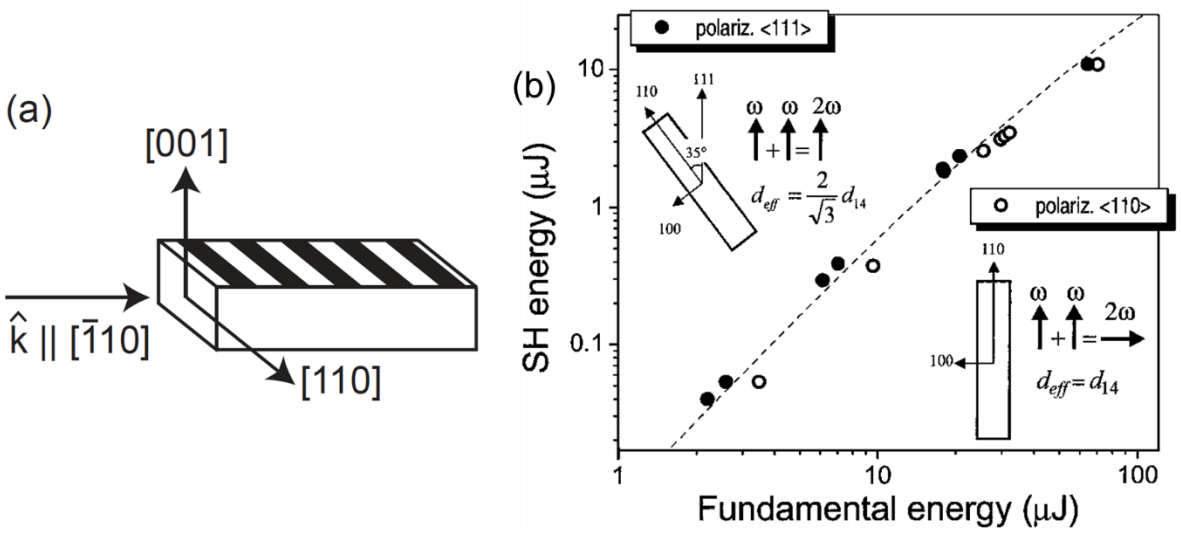

Figure 4. (a) Schematic of the polarization direction of input against the crystal coordinate. (b) The relationship of the fundamental polarization and the second harmonic polarization. [39].

Third-Order Nonlinear Optical Processes

Third-order nonlinear process through $\chi^{(3)}$ media includes third-harmonic generation, four-wave mixing (FWM), intensity dependent refraction, cross phase modulation, two-photon absorption, Raman scattering, and so on. Unlike $\chi^{(2)}$ media, any material including air can have $\chi^{(3)}$ effect.

Z-scan

The Z-scan technique was invented in 1989. The study has been conducted for more than 30 years to measure nonlinear refraction and absorption. This method is rapid, simple, and accurate. A sample of the material under investigation is moved through the focus of a laser beam, and the transmitted light through the aperture is recorded (Figure 5).

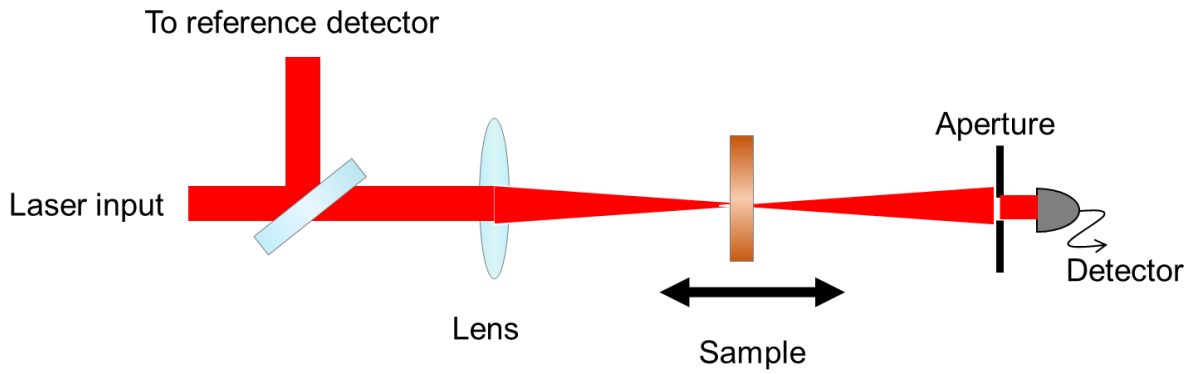

Figure 5: Schematic drawing of the Z-scan technique.

The MPA coefficient and nonlinear refractive index are obtained by analyzing open- and closed-aperture measurements, respectively. If the nonlinear refractive index is positive, and the sample is placed after the focus, self-focusing reduces the beam divergence and thus increases the detector signal. If the sample is moved to the left-hand side of the focus, the focus is moved to the left, and the stronger divergence after the focus decreases the detector signal. From the detector signal depending on the sample position, it is possible to extract the magnitude of the nonlinear index. The nonlinear absorption can also affect the measured signal. This feature can be measured separately by recording the power of the beam without the aperture.

Closed Aperture Z-scan

The nonlinear refractive index is also known as the Kerr effect, which can increase or decrease the refractive index when an intense beam propagates through a medium: $\Delta n = n_2 I(t)$. It is derived by third-order nonlinear polarization for self-phase modulation (SPM). SPM induces the intensity-dependent nonlinear phase shift and shifts the front of pulse to lower frequencies and the back of pulse to higher frequencies Using the cubic nonlinear susceptibility, it is expressed as $n_2 = \frac{3}{4}\frac{\chi^{(3)}}{n^2(\omega)c\epsilon_0}$. The measurement of n_2 is often done with the Z-scan technique, which is based on self-focusing via Kerr lens.

For Z-scan analysis, a Gaussian beam is focused and passes through a thin sample as depicted in Figure 6. The nonlinear phase shift in a sample is multiplied to the original *E*-field $E_e(z,r,t) = E(z,r,t)e^{i\Delta\phi(z,r,t)}$. After the free space propagation of distance d from the exit of the sample, the transmitted power is derived as following

$$T(z) = \int_{-\infty}^{\infty} P_T\big(\Delta\Phi_0(t)\big)\,dt / S\int_{-\infty}^{\infty} P_i(t)\,dt \qquad (2)$$

where P_T is the power at the aperture, S is the aperture linear transmittance and P_i is the input power [40].

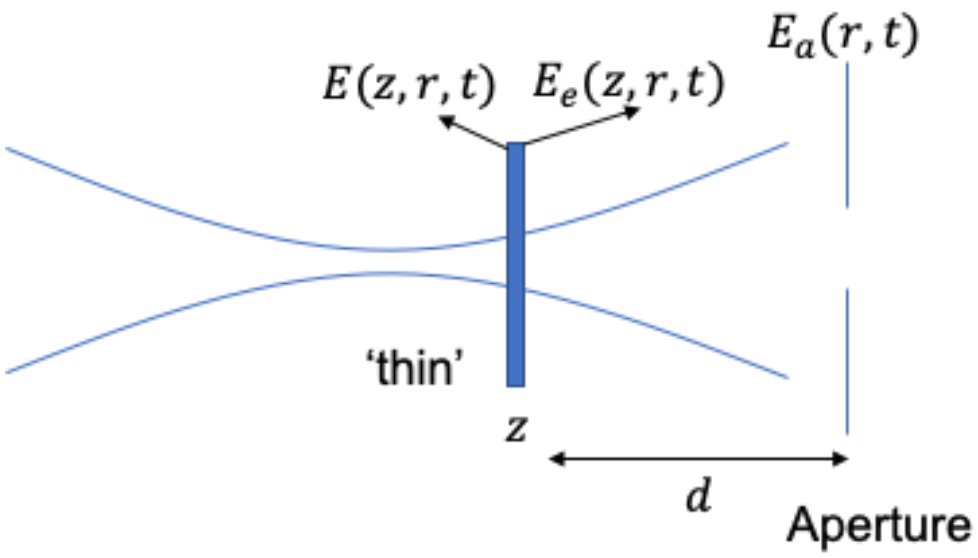

Figure 6. Schematic image of analyzing the nonlinear phase shift in Z-scan.

The numerically calculated Z-scan transmittance curves for both positive and negative sign of n_2 is shown in Figure 7. Using the value of peak to valley and the aperture parameter S, the nonlinear phase shift, the changes of refractive index, and finally the n_2 are obtained.

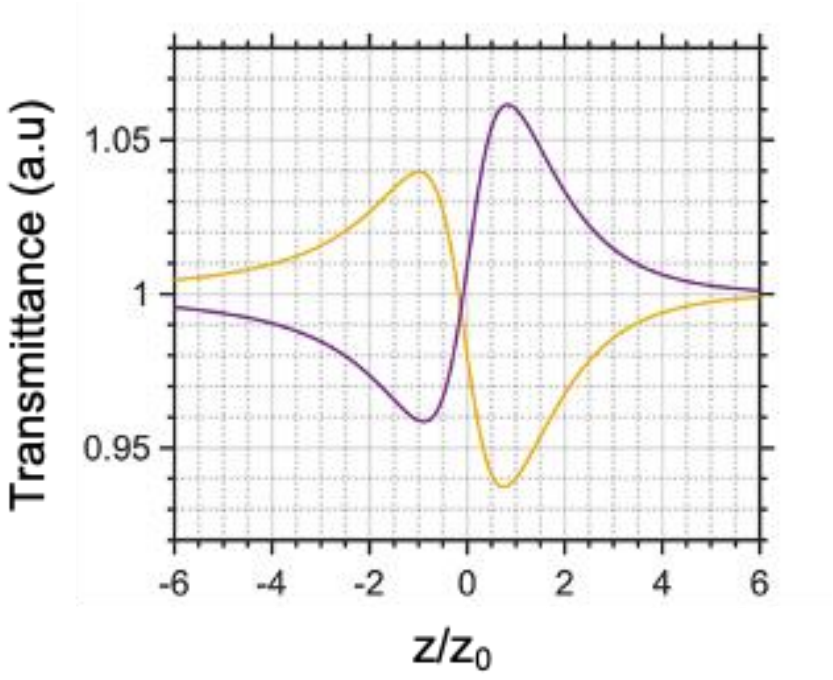

Figure 7. An example of closed aperture Z-scan transmittance curves.

The n_2 at a certain wavelength can be expected from the two-band model for a direct bandgap semiconductor [41] using the data obtained for other wavelengths. Independent of materials, the magnitude of n_2 is dependent on $n_0^2 E_g^{-4}$. This law hints that the magnitude of GaAs is about 5 times higher than that of GaP at 1 μm. Figure 8 shows the calculated n_2 using the parameter $K' = 1.50 \times 10^{-8}$ and the bandgap energy without any fitting. Using the ratio of two wavelengths and taking the value of ref. [26], the n_2 is expected to be $2.1 \times 10^{-18} \mathrm{m}^2/\mathrm{W}$ at 2.35 μm and $1.9 \times 10^{-18} \mathrm{m}^2/\mathrm{W}$ at 4.7 μm.

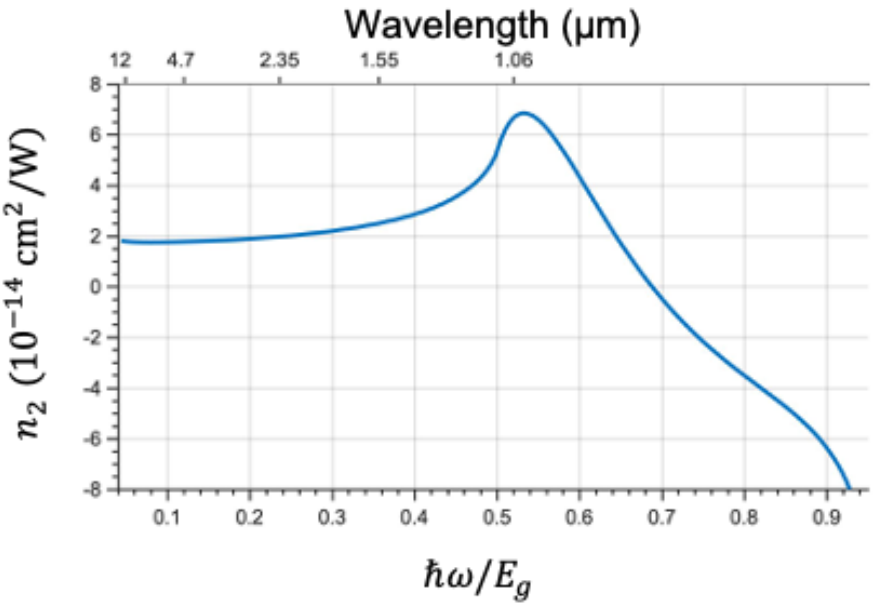

Figure 8. Calculated nonlinear refractive index of GaP as a function of normalized photon energy.

Open Aperture Z-scan

Assuming that only one type of MPA dominates for a given wavelength, the intensity variation along the propagation direction is expressed as

$$\frac{dI(z,r,t)}{dz} = -\alpha_N I^N(z,r,t) \quad (3)$$

where α_N is an *N*-photon absorption coefficient. In the limit of small absorption $(T - T_0)/T_0 \ll 1$, by integrating over space and time the transmittance is calculated to be [42]

$$\frac{T_0}{T} = 1 + \frac{1}{N^{3/2}} \alpha_N I_{in}^{N-1} l \quad (4)$$

where T/T_0 is normalized transmission. In data processing, MPA coefficients are deduced by best fitting to the Eq. (4).

Z-scan for Thick Samples

Thick sample analysis in Z-scan must be considered for the sample longer than the depth of focus. This method is used when it is necessary to focus away from the damage prone surfaces, or the laser is not powerful and requires thicker sample length to increase the nonlinear effect.

Anisotropy of 3rd Order Nonlinearity in Zincblende Structures

Although in the application of broadband QPM based OPO, the polarization is always fixed along [1 1 1] direction to maximize the second-order nonlinear coefficient, it is important to know the degree of anisotropy, which is necessary to obtain a threshold for all-optical switching, for example. The theory of the anisotropy in zinc-blende semiconductors is given by [43] for two-photon absorption and by [44] for nonlinear refractive index. In the experiment, strong anisotropy and crystal orientation dependence of the nonlinear processes have been reported in GaAs at 2 μm [42] and GaP at 1.04 μm [26].

The third-order susceptibility tensor has 21 nonzero elements and 4 of which are independent. If a material is isotropic, there is a relationship between the four independent tensor elements that $\chi^{(3)}_{xxxx} = \chi^{(3)}_{xxyy} + \chi^{(3)}_{xyyx} + \chi^{(3)}_{xyxy}$. The anisotropy parameter is defined as bellow.

$$\sigma = \frac{\chi^{(3)}_{xxxx} - \left(\chi^{(3)}_{xxyy} + \chi^{(3)}_{xyyx} + \chi^{(3)}_{xyxy}\right)}{\chi^{(3)}_{xxxx}}. \quad (5)$$

The following analysis applies for both two-photon absorption and nonlinear refractive index, therefore the discussion here follows the latter case. For arbitrary polarization incident in a single beam configuration, n_2 is expressed as

$$n_2 = \frac{3}{4\epsilon_0 c n_0^2} Re\left\{\chi^{(3)}_{xxxx}\right\}\left[1 - \sigma + \sigma \sum_i |e_i|^4\right] \quad (6)$$

where e_i is a unit vector of input polarization and $i = x, y, z$ (crystal frame). In the crystal coordinate system used for the OPOs, where $\hat{e} = \frac{\sin\theta}{\sqrt{2}}(\hat{x} - \hat{y}) + \cos\theta\,\hat{z}$, the effective third-order susceptibility is given by

$$\chi^{(3)}_{\text{eff}} = \chi^{(3)}_{xxxx}\left[1 - \frac{\sigma}{2}(1 + 3\cos^2\theta)\sin^2\theta\right] \quad (7)$$

The calculated $\chi^{(3)}_{\text{eff}}$ is shown in Figure 9. The maximum value is taken when the input polarization angle is 55˚, where, for example in GaAs, the bond of Ga-As is parallel to the polarization angle.

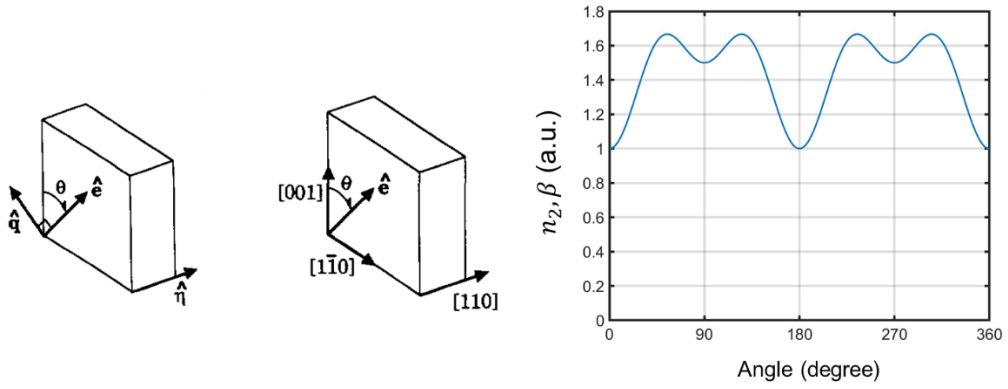

Figure 9. Definition of the coordinate system and the calculated $\chi^{(3)}$ for different input polarization angle.

CHAPTER THREE:
RANDOMLY PHASE MATCHED FREQUENCY CONVERSION MODEL IN ZINCBLENDE POLYCRYSTALS FOR ULTRAFAST INTERACTIONS

Introduction

Phase matching is a critical factor for generating new optical frequencies in the coherent process of nonlinear optical frequency conversion [38]. Birefringent crystals have been widely used to compensate phase mismatch, while quasi phase matching (QPM) is another technique to maintain growth of a new optical field by preventing destructive interference. An alternative approach is random phase matching (RPM), which avoids destructive interference by exploiting the random nature of disordered crystalline domains. A wide variety of materials can show this feature if they are composed of disordered microstructures. In the early stage of laser development, RPM has been used in a powder technique for evaluating nonlinear optical materials [36]. The first frequency conversion in a polycrystalline semiconductor where monocrystals are embedded with random orientations was demonstrated in 1966 and the variation of an output signal in terms of intensity and polarization has been qualitatively discussed [32]. Thanks to the fact that disordered materials have extremely wide acceptance bandwidth they have been used as a nonlinear gain medium for several applications such as nonlinear optical microscopy, autocorrelation measurements, sum- and difference-frequency generation.

In the field of ultrafast interactions, a full advantage has been taken of the ultra-wide bandwidth of nonlinear interactions in polycrystalline zinc-blende materials. A spectrally broad second harmonic generation (SHG) with a high power of 0.3 W and a number of other nonlinear wave mixing has been observed with the gain medium of polycrystalline Cr^{2+}:ZnS and Cr^{2+}:ZnSe

in mode-locked lasers [45]. Recently in our group, an optical parametric oscillator (OPO) based on RPM was demonstrated in a disordered ZnSe ceramic material, pumped by femtosecond 2.35 μm laser pulses. The OPO produced an ultra-broad spectrum spanning 3-7.5 μm and exhibited pump depletion as high as 79% [29]. Multi-octave spectrum via simultaneous randomly phase matched three-wave mixing processes, facilitated by filamentation, was also observed in polycrystalline ZnSe [46].

RPM can be viewed as an analogy of a random walk, where the electric field grows as the square root of the interaction length within a nonlinear material. Thus, in RPM an output intensity increases linearly with a sample thickness. Another feature is that the optimum average grain size for high conversion efficiency is the same as coherence length for a three-wave interaction [33,47–49]. Although there are several attempts to analytically describe the frequency conversion process based on RPM, none of them rigorously derived the probability distribution of the effective nonlinear susceptibility of randomly rotated crystal; also, polarization analysis in RPM has been dismissed in these works. Additionally, most papers assume that the beam size is larger than the average grain size. In ultrafast OPO applications that we are most interested in, the focused beam size inside a polycrystalline material is usually smaller than the average grain size and statistical averaging over a beam aperture no longer applies, since the beam will typically see only one grain at a time. In this chapter, we present a model for ultrafast nonlinear $\chi^{(2)}$ interactions in an RPM material that includes random grain orientation, realistic grain size distribution, as well as variation of the output polarization due to randomly transformed susceptibility tensor. The SHG process is used for the analysis since SHG and subharmonic OPO is related to each other through effective second-order nonlinearity in a three-wave mixing process [37].

Second-Order Nonlinear Susceptibility in a Single Crystal with Arbitrary Orientation

The susceptibility variation in each grain is modeled by randomly rotated crystal coordinates with respect to a fixed laboratory frame. Since polycrystals are an ensemble of monocrystals with random orientation, it is reasonable to start with an arbitrarily oriented single crystal. There are several ways to orient a crystal randomly. Here we show the way of selecting random crystal orientation in an intuitive way as shown in Figure 10. The random orientation of a crystal corresponds to a random rotation of a crystal coordinate. The random rotation of the coordinate is described as follows. First, setting a uniformly distributed point (x_0, y_0, z_0) on a unit sphere. Secondly, rotating a coordinate for one of the principal axes (z-axis) to direct the point. Thirdly, rotating the coordinate about the vector $\vec{n}_3 = (x_0, y_0, z_0)$ by ψ uniformly from 0 to 2 π. The uniformly distributed point on the sphere is expressed as $(x_0, y_0, z_0) = (\sin\phi\cos\theta\,, \sin\phi\sin\theta\,, \cos\phi)$ with the probabilities of $\theta \in [0, 2\pi)$ and $\phi = \arccos(u)$ where $u \in [-1\ 1]$. These operations are summarized as three successive rotations $R_{\vec{n}_1}(\theta), R_{\vec{n}_2}(\phi)$ and $R_{\vec{n}_3}(\psi)$, which are denoted as Rodrigues' rotation formula corresponding to a rotation by an angle ϕ about a fixed axis specified by the unit vector $\vec{n}_2$ for example. For a given point the matrices are defined by $\vec{n}_1 = (0,0,1)$, $\vec{n}_2 = (-\sin\theta\,, \cos\theta\,, 0)$ and $\vec{n}_3 = (x_0, y_0, z_0)$.

$R = R_{\vec{n}_3}(\psi)R_{\vec{n}_2}(\phi)R_{\vec{n}_1}(\theta) =$

$$\begin{pmatrix} \cos\phi\cos\theta\cos\psi - \sin\phi\sin\psi & -\cos\phi\cos\theta\sin\psi - \cos\psi\sin\phi & \cos\phi\sin\theta \\ \cos\theta\cos\psi\sin\phi + \cos\phi\sin\psi & -\cos\theta\sin\phi\sin\psi + \cos\phi\cos\psi & \sin\phi\sin\theta \\ -\cos\psi\sin\theta & \sin\theta\sin\psi & \cos\theta \end{pmatrix} \quad (8)$$

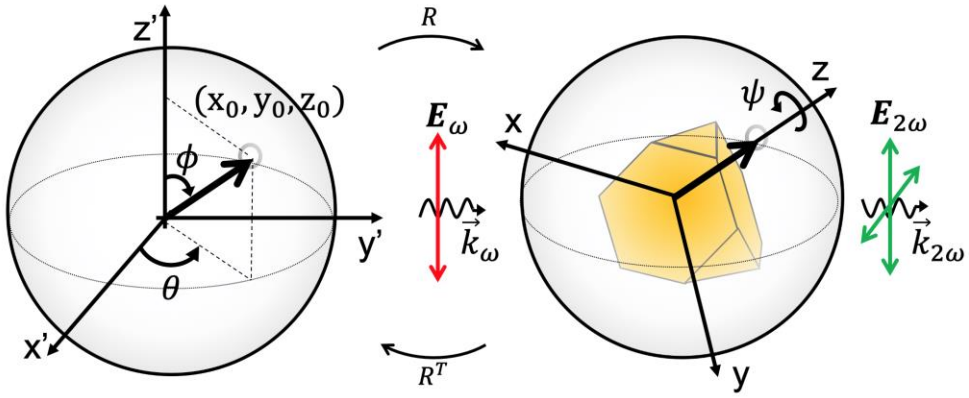

Figure 10. Schematic of the random rotation from a laboratory coordinate to a crystal coordinate and vice versa. The incoming light propagates along the y' axis, while its polarization is along z' axis.

The susceptibility of randomly oriented crystal is found in the process of deriving the nonlinear polarization in the laboratory frame for a certain crystal orientation. In two Cartesian coordinates (x, y, z) as a crystal and (x', y', z') as a laboratory, the nonlinear polarizations are connected by the rotation matrix as $P_{i'}^{(2)'} = R_{i'i}^T P_i^{(2)}$ (and likewise for electric fields). Since the rotation matrix is an orthogonal matrix, the relationship is also described as $E_j = R_{j'j}^T E_{j'}'$. Thus, the nonlinear polarization in the laboratory frame has the transformed nonlinear susceptibility tensor that is computed by the transformation rule for the third rank tensors $\chi_{i'j'k'}^{(2)'} = R_{i'i}^T R_{j'j}^T R_{k'k}^T \chi_{ijk}^{(2)}$ derived as follows.

$$P_{i'}^{(2)'} = R_{i'i}^{T}\epsilon_0 \int_{-\infty}^{\infty}\int_{-\infty}^{\infty} d\omega_1 d\omega_2 \; \chi_{ijk}^{(2)} E_j(\omega_1)E_k(\omega_2)e^{-i(\omega_1+\omega_2)t}$$

$$= R_{i'i}^{T}\epsilon_0 \int_{-\infty}^{\infty}\int_{-\infty}^{\infty} d\omega_1 d\omega_2 \; \chi_{ijk}^{(2)} R_{j'j}^{T} E'_{j'}(\omega_1) R_{k'k}^{T} E'_{k'}(\omega_2)e^{-i(\omega_1+\omega_2)t} \quad (9)$$

$$= \epsilon_0 \int_{-\infty}^{\infty}\int_{-\infty}^{\infty} d\omega_1 d\omega_2 \; \chi_{i'j'k'}^{(2)'} E'_{j'}(\omega_1)E'_{k'}(\omega_2)e^{-i(\omega_1+\omega_2)t}.$$

In the contracted form of input polarizations for SHG, assuming that the fundamental electric field is linearly polarized, the second-order polarization that is parallel and perpendicular to the input polarization is given as

$$\begin{pmatrix} P_{||}^{(2)'}(2\omega) \\ P_{\perp}^{(2)'}(2\omega) \end{pmatrix} = \epsilon_0 E^2(\omega) d_{14} \begin{pmatrix} 6R_{11}R_{21}R_{31} \\ 2R_{11}R_{21}R_{32}+2R_{11}R_{22}R_{31}+2R_{12}R_{21}R_{31} \end{pmatrix}, \quad (10)$$

where d_{14} is the only nonzero component in the tensor for the $\bar{4}3m$ point group, and the resulting effective nonlinear coefficient for both parallel and perpendicular polarization is modified by the coordinate rotation.

A Monte Carlo simulation of one million iterations of random rotations yields the distribution of the nonlinear coefficient in a randomly oriented single crystal for both parallel and perpendicular output polarizations with respect to the linearly polarized incoming electric field as shown in Figure 11(a). The nonlinear coefficient fluctuates within the expected range, $|d_{||}/d_{14}| \leq \sqrt{4/3}$ for the parallel case, and $|d_{\perp}/d_{14}| \leq 1$ for perpendicular case [39,50,51]. The expectation value of the magnitude of the nonlinear coefficient in a single grain is $0.48d_{14}$ for parallel and $0.41d_{14}$ for perpendicular output polarizations. Figure 11(b) shows that some grains do not even induce the polarization contributing to the light propagating direction but there is a decent

probability for the grains to align with [1 1 1] direction, which maximizes the nonlinearity for the given input polarization.

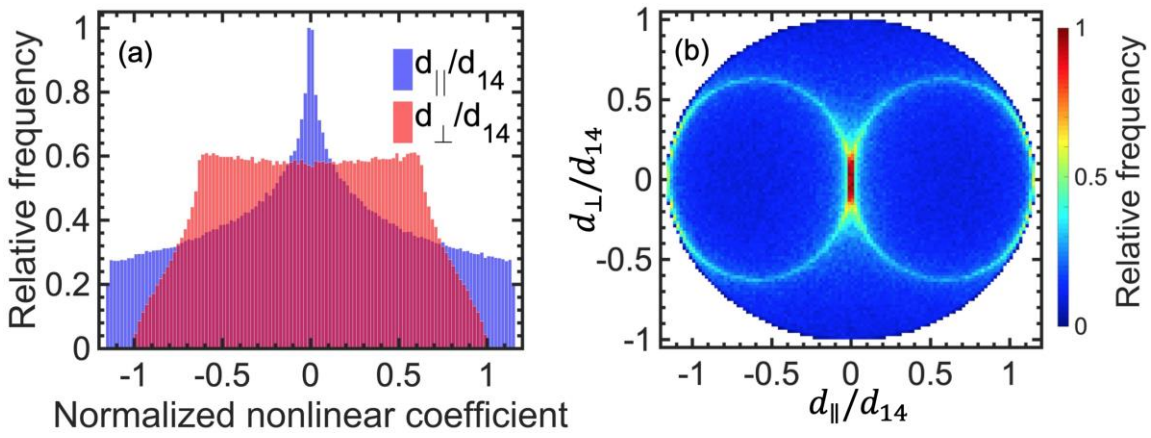

Figure 11. (a) Probability of normalized effective nonlinear coefficient in a randomly oriented single crystal for the parallel (blue) and perpendicular (red) output polarization. (b) Correlation of the nonlinear coefficient between orthogonal polarizations. Both figures are plotted with the bin size of 0.02.

Considering the second harmonic intensity after a single grain, where the contribution of nonlinear coefficient is expressed as a square of it, the effective squared nonlinear coefficient on average is $0.34d_{14}^2$ for the parallel and $0.23d_{14}^2$ for perpendicular polarization. Figure 12 shows the histogram of squared effective nonlinear coefficient including the combined (parallel and perpendicular) one. The total averaged nonlinear coefficient has 18% probability to have the higher intensity compared to the case where the polarization is along [1 1 0] direction. The values of these nonlinear coefficients are summarized in Table 1.

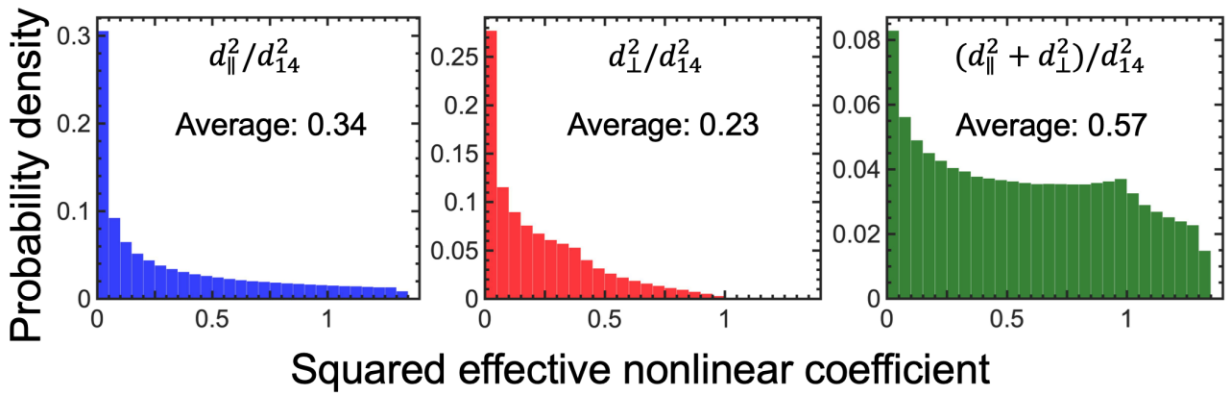

Figure 12. Probability of normalized squared nonlinear coefficient for parallel (blue), perpendicular (red) and their combined (green) output polarization with the bin size of 0.05.

Table 1: Summary of magnitude of nonlinear coefficients for different polarization outputs

$\lvert d_{\lvert\rvert}/d_{14}\rvert$	$\lvert d_{\perp}/d_{14}\rvert$	$d_{\lvert\rvert}^2/d_{14}^2$	$d_{\perp}^2/d_{14}^2$	$(d_{\lvert\rvert}^2 + d_{\perp}^2)/d_{14}^2$
0.48	0.41	0.34	0.23	0.57

SHG Experiment

We characterized the nonlinear optical properties of ZnSe ceramics through SHG process (from 4.7 to 2.35 μm) using a nanosecond OPO source at λ = 4.7 μm. The OPO was pumped by a λ = 1.064 μm Q-switched Nd:YAG laser (Spectra-Physics Model T40-X30S) with 20 ns pulse duration and 1.5 mJ pulse energy operating at 100 Hz repetition rate. A tunable flat-flat

periodically poled lithium niobite (PPLN) OPO linear cavity produced linearly polarized idler wave with an energy of about 15 µJ, which was normally focused into the sample after removing the pump beam and the OPO signal. The experimental setup is shown in Figure 13. The samples were mounted on an XY translation stage, and the SH power for parallel and perpendicular polarizations was 2D mapped with 100-µm steps. The pump beam size was 50 µm at the focus and the Rayleigh length was longer than the crystal thickness.

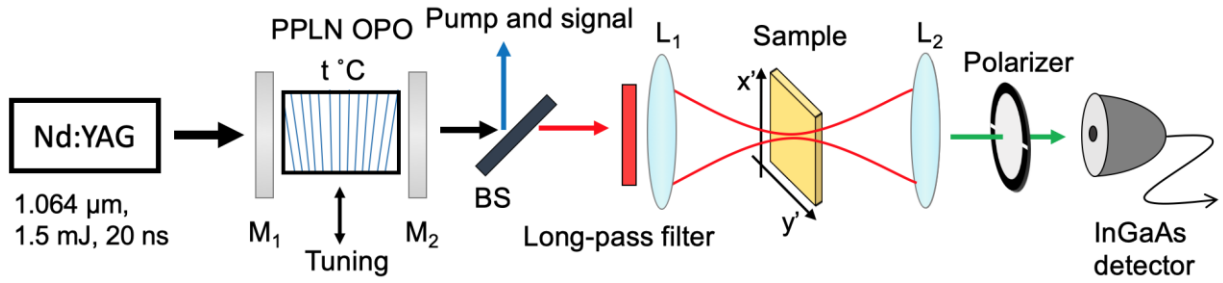

Figure 13. Experimental setup for the characterization of polycrystalline ZnSe via SHG. PPLN OPO was tuned to select the idler wave of 4.7 µm. The beam splitter (BS) rejected the OPO signal wave and the pump beam and transmitted the OPO idler wave. The beam was focused by the f = 50 mm CaF2 lens (L1). A ZnSe sample was placed in the focus and scanned in x-y directions. The SH signal was collected by the f = 50 mm BK7 lens (L2) and measured using an InGaAs detector

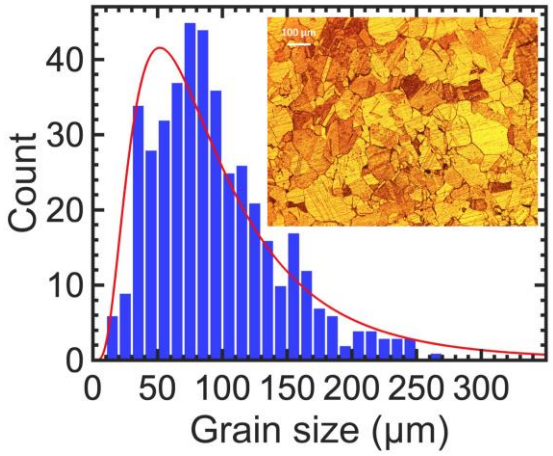

Figure 14. Grain size distribution in the real sample by the line intercept method. Inset: 1.2 mm x 0.9 mm cross section of a chemically etched ZnSe sample.

The samples we used in the experiment were obtained from IPG Photonics. They were based on commercial CVD-grown ZnSe ceramic, where the optimal average grain size of ~100 μm – close to the coherence length of our studied nonlinear processes – was achieved by thermal annealing in vacuum at 900 ˚C. The samples were polished with 5 x 10 mm cross section, and their thickness varied between 0.5 to 2 mm. The surface of a chemically etched sample and its grain size distribution is shown in Figure 14. The grain size was measured by the linear intercept method using a microscope. The average grain size was 95 μm and the standard deviation is 48 μm, and lognormal fitting had an average value of 100 μm and a median value of 80 μm.

A typical mapping result for 1-mm-long sample with hot spots (higher gain points of a sample) for both parallel and perpendicular output polarizations and its distribution is shown in Figure 15(a,b). Some points produced much higher SH power and these hot spots can be used for applications requiring high nonlinear gain. The SH power ratio of parallel and perpendicular $P_{||}^{2\omega}/P_{\perp}^{2\omega}$ at each point can vary from zero to infinity. Their average values however give the ratio

from 1.2 to 2.1 for several samples. Interestingly, when the sample was rotated by 90˚ on the transverse plane, the ratio takes the symmetry value to about 1.5 in that range, which is in accord with the simulated average ratio 1.5. This result indicates that the grain size and its orientation are not purely random. This can be due to possible anisotropy of CVD-grown ZnSe (e.g. grains that are elongated in one direction), associated with a certain growth direction. Figure 15(c) plots the average SH power for different lengths of samples, which are all from the same origin. The linear dependence on the sample length confirms the prediction of the RPM theory.

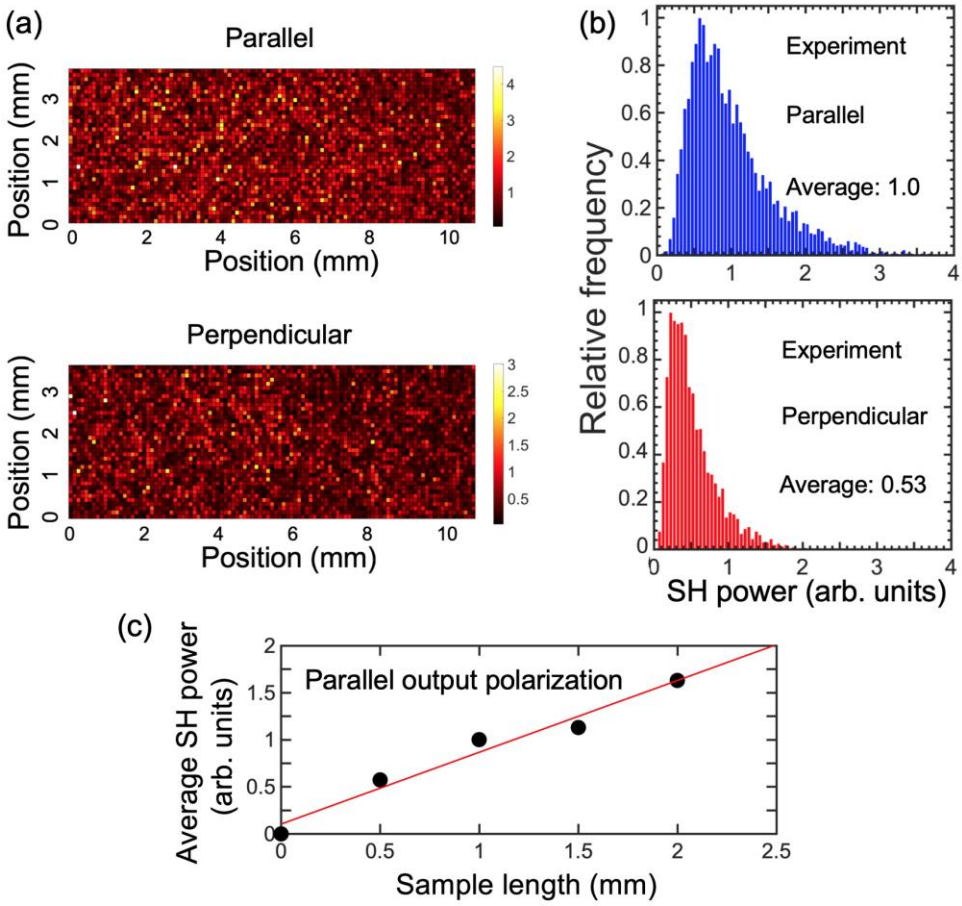

Figure 15. (a) Normalized SH power scanned over a sample with 100-μm step for both parallel and perpendicular polarizations, where one can see SH hot spots. (b) Histogram of SH power for both polarizations. The average SH power of parallel output polarization is normalized to be 1, where that of perpendicular one varies from 0.48 to 0.83 in different samples. (c) Average SH power with different lengths of samples.

SHG Model in Random Phase Matching

RPM is numerically investigated in two conditions in terms of the beam size *w* compared to the average grain size *D*. The modeled polycrystalline structure is created by Voronoi tessellation [52] and is based on a real ZnSe sample in terms of the distribution of the grain size

and orientation. The grain size distribution by the linear intercept method in the generated structure had the lognormal fitting with the mean and median values of 100 μm and 80 μm respectively, which is the same distribution as the one obtained from the cross section of real samples. After the volume of 0.5 mm x 0.5 mm x 1.0 mm is created, a randomly picked up structure of 1 mm thickness is used for the simulation. The formulas used in this simulation are shown below, where d_m is the calculated nonlinear coefficient for a grain number m and z_m is the starting point in the propagation direction for m^{th} grain. The total SH electric field is the sum of the SH generated in each grain.

$$E_{\parallel}(z, 2\omega) = \frac{i\omega}{n_{2\omega}c} E^2(\omega) \sum_m d_{m,\parallel} \int_{z_{m-1}}^{z_m} e^{i\Delta kz}\, dz \qquad (11)$$

$$E_{\perp}(z, 2\omega) = \frac{i\omega}{n_{2\omega}c} E^2(\omega) \sum_m d_{m,\perp} \int_{z_{m-1}}^{z_m} e^{i\Delta kz}\, dz \qquad (12)$$

The grain size distribution and the modeled structure are shown in Figure 16(a). The random susceptibility tensor is assigned to each grain and single or multiple (assuming that the polarization induced in each grain is uncorrelated in a transverse plane) 1D simulation along the beam propagation direction is performed inside the structure of the beam size volume. First, when the beam size is much smaller (ignoring multiple grains on transverse plane) than the average grain size, which typically is the case for ultrafast interactions, the SH power has larger overall fluctuation and hence larger maximum value although it has a higher possibility of producing weak SH power as shown in Figure 17(a). Secondly, when the beam size is comparable to the grain size (a plane wave with FWHM of 50 μm is assumed), the simulated SH power varies in the form of lognormal distribution as shown in Figure 17(b). Comparing Figure 15(b) and Figure 17(b), the simulated SH power histogram that takes averaging over the beam cross section into account

demonstrated good agreement with the experiment in terms of the histogram shape and the ratio of parallel and perpendicular polarization outputs. This smaller number of weak SH power is due to the effect of multiple grains, where the average number of 35 grains including tiny ones contributes to producing the SH signal (one of the corresponding structures is shown in Figure 16(b)). For both cases the parallel SH power is stronger by 1.5 times and their average values are the same. 10,000 set of different structures is tested, and maximum efficiency reaches at least 4 or more times larger than the average efficiency for this interaction length. It can be expected that when a beam passes through a large number of grains ($w >> D$) the variation of the signal is reduced due to the averaging effect across multiple grains.

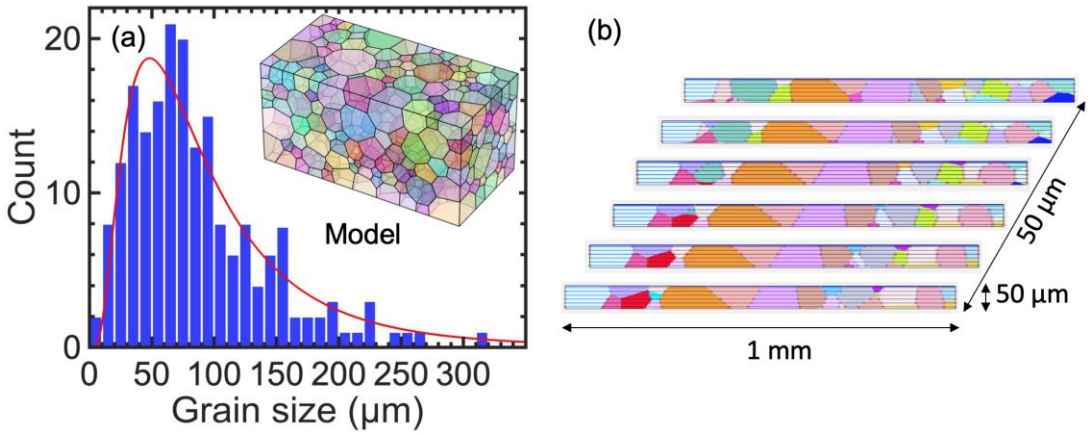

Figure 16. (a) Grain size distribution in the simulated structure which is measured using the line intercept method. Inset: a polycrystalline structure model created by Voronoi tessellation. Different colors show the different orientations of grains. (b) An example of a 50 μm x 50 μm which is randomly cut from the modeled structure.

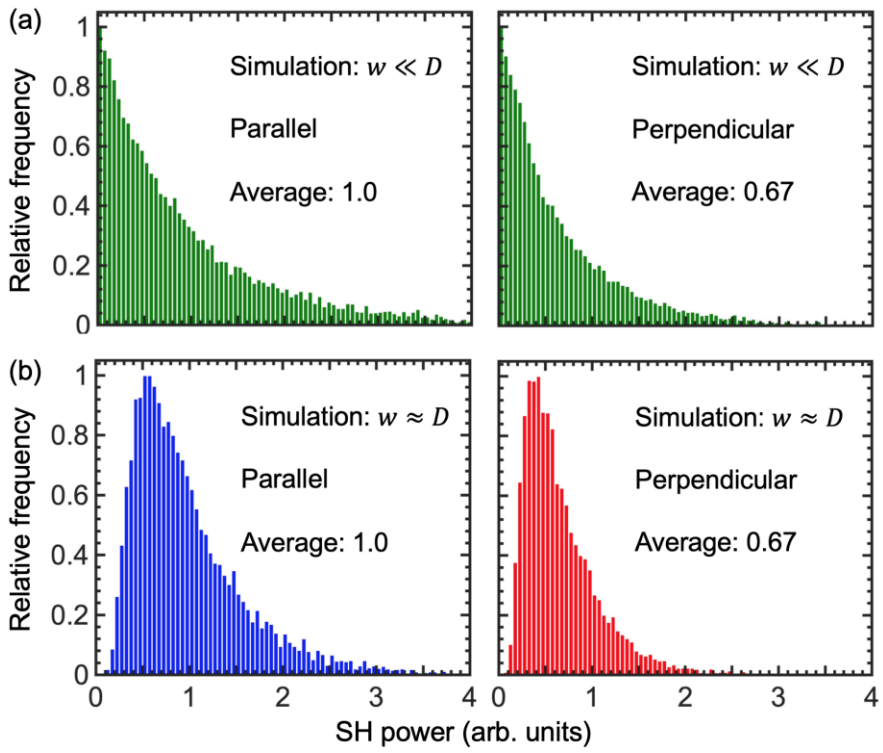

Figure 17. Simulated histograms of normalized SH power of the parallel and perpendicular components in the cases of (a) $w << D$ and (b) $w \approx D$.

The probability of output polarization state is examined in the case of $w << D$. The polarization state after propagating 200 μm and 1.0 mm for the coherence length of 100 μm is shown in Figure 18. When the average grain size is close to L_c, the electrical field is likely to evolve with changing the phase with only 0 or π in every boundary of grains. For the interaction length of only a few L_c SH signal tends to have a linear polarization because the phase between parallel and perpendicular component is close to 0 or π. As the interaction length gets longer, the fluctuation of grain size and the nonlinear coefficient let electrical field evolve in an arbitrary

direction in a complex plane and thus the phase between parallel and perpendicular components becomes random.

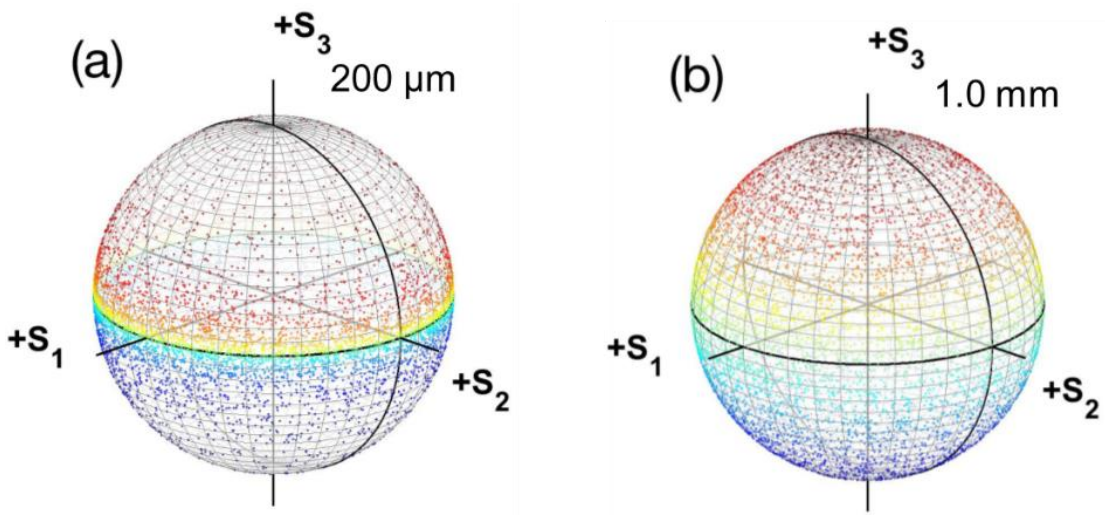

Figure 18. The evolution of output polarization of SH field illustrated on Poincare sphere. The principal axis shows the Stokes parameters. Each point on the sphere represents the polarization state by Monte Carlo, and points are linearly colored along the axis of S_3.

RPM Performance Compared to QPM

As demonstrated before RPM is very well suited for ultrafast three-wave interactions. In fact, the group delay walk-off between the waves with different wavelengths, especially when few-cycle pulses are used, limits the interaction length to less than 1 mm. Here, we evaluate the performance of RPM in ZnSe by comparing it with QPM in the case of an ultrafast interaction. We modeled an ideal ZnSe QPM material, which used nonlinear coefficient of $\sqrt{4/3}d_{14}$. For the

same sample length, the SH power in RPM is compared with the one in QPM as shown in Figure 19, indicating that with a small number of grains there is a greater chance that RPM can perform on par with a QPM. In a separate ultrafast OPO experiment, it is shown that by using hot spots the OPO threshold for an RPM ZnSe sample with 5-10 coherence length is 90 mW, while that of oriented patterned GaAs in a similar OPO arrangement is 8 mW. Since the nonlinear figure of merit in GaAs is 6.5 times larger (at Brewster angle operation) it is calculated that the parametric gain in RPM ZnSe is close (to within less than a factor of 2) to the one for an ideal QPM sample with the same length. As the modeling shows, for this small number of grains participating, the threshold is in the range of consistency. The polycrystalline ZnSe is a great candidate as the gain medium for a femtosecond laser source especially because the QPM ZnSe is not yet available.

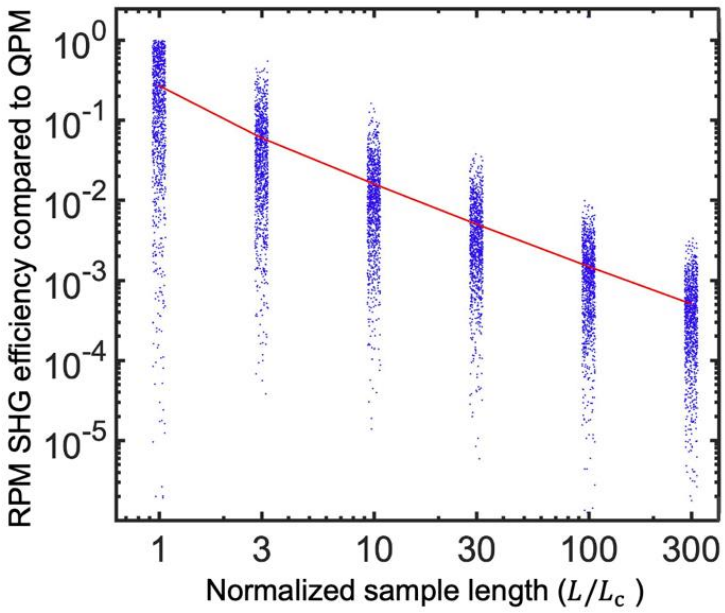

Figure 19. RPM SHG efficiency normalized to QPM efficiency (only parallel output component is counted) verses normalized sample length. For each sample length (1, 3, 10, 30, 100, 300 L_{coh}), Monte Carlo simulation is performed using 1,000 sets of random structure and the average efficiency is shown with the solid line. Nonlinear coefficient of $\sqrt{4/3}d_{14}$ is used in the QPM condition.

CHAPTER FOUR:
NUMERICAL SIMULATION FOR BROADBAND MID-INFRARED OPTICAL PARAMETRIC OSCILLATORS

Introduction

Mid-infrared frequency comb sources have been providing rich and quantitative information of molecules by using various spectroscopic techniques. For spectroscopic detection of a mixture of multiple species, one needs a spectrally broad comb with enough power. Yet, fulfilling these metrics simultaneously has been challenging. The exploration of suitable laser sources is particularly active recently, and full transparency range of materials are now being exploited in various approaches through nonlinear frequency conversion. Intra-pulse difference frequency generation (IDFG) exhibits a simple scheme after preparing amplified and/or temporally compressed high-power pump pulses. The spectra seamlessly cover throughout longwave portion of the mid-infrared range in different kind of nonlinear media, such as $LiGaS_2$, OP-GaP, $ZnGeP_2$, GaSe, and polycrystalline ZnSe/ZnS [7–10,25]. Although the spectrum spans more than an octave wide, the mid-infrared output power is limited due to the low conversion efficiency. The spectrum components generated by IDFG have zero carrier-envelope offset (CEO), however, the generated spectrum by a cascaded interaction with pump laser pulse can have different CEO component, thus not a single frequency comb. Supercontinuum (SC) generation in nanophotonic waveguides made from silicon or silicon nitride generates broadband mid-infrared combs reaching the longwave cutoff of the material [17]. They operate with small input pulse energy, and group-velocity-dispersion (GVD) engineered structure controls the spectral shape, but the spectral density distribution is strongly uneven. Microresonator-based Kerr frequency combs present compact and robust system, yet the spectrum coverage is limited to the wavelengths around the CW pump laser.

Each MIR comb source has its advantages and drawbacks. In terms of spectral bandwidth, accessible MIR output power and coherency, optical parametric oscillators (OPOs) have been holding the promise for real-world applications. Among them, a synchronously pumped subharmonic OPO demonstrates instantaneous broad bandwidth and most importantly the down-converted comb inherits the coherence property of the pump combs [53,54].

Thanks to the intensive study and development of mode-locked Cr:ZnS/ZnSe lasers of watt-level average power, the accessible power of MIR range will certainly increase owing to relatively high conversion efficiency of frequency down-conversion in OPOs. With the combination of newly developed nonlinear medium OP-GaP, which has zero group velocity delay around the half frequency of the pump laser (center wavelength of 2.35 μm), and the injector that injects pump beam into a cavity without introducing extra phase, the broad spectrum (3-12 μm) in a resonant system is achieved [55].

This high-intensity pump pulses may lead a complex spectrum broadening process beyond the conventional $\chi^{(2)}$ subharmonic OPO due to the third-order nonlinear susceptibility $\chi^{(3)}$ effect. With increasing pump intensity, the intensity dependent phase shift and four-wave mixing effect play a significant role in the pump pulses and accordingly for the circulating mid-infrared pulses, which is similarly observed in high-power picosecond OPO [56]. In the case of degenerate femtosecond OPOs, it may extend the spectrum to the longwave cutoff of materials, or the spectrum would merge and become indistinguishable to the pump laser.

In this work, we model broadband mid-infrared combs in a minimally dispersive cavity based on OP-GaP crystal. Taking the parameters from the recently demonstrated experiment, the

simulation result is compared with the experimental result, especially focusing on the role of $\chi^{(3)}$. Furthermore, the simulation predicts the time-domain profiles of OPO waveform.

Nonlinear Single-Wave Propagation Model in an Optical Parametric Oscillator

To simulate the evolution of the OPO pulses, we used an approach based on the nonlinear wave equation in the frequency domain, which treats all the interacting waves, including the OPO, pump, sum frequency (SF), and second harmonic (SH), as a single field and describes the dynamics of the electric field rather than that of the envelope [57,58]. The commonly used approach to distinguish waves by their spectral bands, so-called coupled-wave equation, is impractical here. The limitation to certain wavelength bands would intrinsically suppress unpredicted mixing products generated by cascaded processes or dismiss the dissipation of pump energy to higher frequency regime in down-converting OPO system, for example. Using this method in prior research, for instance, the formation and interaction of few-cycle soliton and the octave spanning pulses by cascaded nonlinear process are demonstrated [59,60]. This method is more suitable to simulate our ultrabroadband subharmonic OPO pulses for the reasons that (i) there are several overlapping spectral bands, e.g. between the pump laser and the OPO, and (ii) the nonlinear crystal can provide simultaneous phase-matching for multiple $\chi^{(2)}$ (including cascading) and $\chi^{(3)}$ (intensity-dependent phase shift and four-wave mixing) nonlinear processes. The key point of this equation's derivation from Maxwell's equation is that the approximation is based on slowly evolving wave approximation (SEWA), physically meaning that the envelope of electric field and the relative carrier phase must not significantly vary as the pulse covers a distance equal to the wavelength

$\lambda_0 = 2\pi c/\omega_0$. In return, it does not explicitly impose a limitation on the pulse or spectral width, which is the requirement of frequently used approach: slowly varying envelope approximation (SVEA). Assuming that all the interacting waves are co-polarized, and under plane-wave approximation, the evolution of the circulating electric field in the nonlinear medium is described, in the frequency domain:

$$\frac{\partial \tilde{E}(z,\omega)}{\partial z} + ik(\omega)\tilde{E}(z,\omega) = -i\frac{\omega}{2\epsilon_0 cn(\omega)}\tilde{P}^{\mathrm{NL}}(z,\omega), \tag{13}$$

$$\tilde{P}^{\mathrm{NL}}(z,\omega) = \epsilon_0\left(\chi^{(2)}\mathcal{F}\{E(z,t)E(z,t)\} + \chi^{(3)}\mathcal{F}\{E(z,t)E(z,t)E(z,t)\}\right), \tag{14}$$

where $E(z,t)$ is the time-domain E-field, $\tilde{E}(z,\omega)$ is the frequency-domain E-field, $\tilde{P}^{\mathrm{NL}}(z,\omega)$ is the nonlinear induced polarization in the frequency domain, $k(\omega)$ is the wavevector module in the medium, c is the speed of light in vacuum, ϵ_0 is the vacuum dielectric permittivity, $n(\omega)$ is the refractive index, $\mathcal{F}\{\}$ represents Fourier transform, and $\chi^{(2)}$ and $\chi^{(3)}$ are quadratic and cubic nonlinear susceptibilities, respectively. It is noted that the frequency domain has a range $(-\infty, \infty)$, and the wave vector $k(\omega)$ has its content in negative frequency, which is the complex conjugate of that in positive frequency. This set of equations can be numerically solved by split-step Fourier method. For each propagation step of Δz, it switches between the time and frequency domains to calculate nonlinear interaction and linear propagation (dispersion and absorption) respectively.

At the exit of the nonlinear medium ($z = l$), the pulse proceeds to a linear propagation in the cavity with dispersion and loss (including the one for the output coupling). The feedback loop is closed when a new pump field is added to the existing field, starting a next roundtrip.

$$\tilde{E}^{(m)}(0,\omega) = \sqrt{R_{inj}(\omega)}\tilde{E}_{\mathrm{in}} + \sqrt{1-R_{inj}(\omega)}\sqrt{1-loss}\; e^{i\phi(\omega)}\tilde{E}^{(m-1)}(l,\omega) \tag{15}$$

Here m indicates the roundtrip number, $R_{inj}(\omega)$ is the intensity reflection coefficient of the injector and *loss* is the combined intensity loss in the cavity from the outcoupling, gold mirrors, scattering, and $\phi(\omega)$ is an extra phase because of the cavity-length mismatch and dispersion of the intracavity elements other than the nonlinear medium.

Numerical Calculation

A quantum noise (1 photon per mode) was added in the frequency domain as an input for the first roundtrip to initiate the parametric process. The calculation was stopped when the change of the current and former roundtrip pulses is negligible, which is approximately 50-150 roundtrip depending on the cavity length. With the time/frequency grid points of 2^{15} and propagation length of 500 μm, the computation for one roundtrip takes a few seconds.

The parameters used in the simulation are completely based on the experiment. The schematic of experimental setup is shown in Figure 20. The input pulse was a hyperbolic secant function with the center wavelength of 2.35 μm and the pulse duration of 62 fs. The peak cross-section-averaged incoming pump peak intensity was set to 50 GW/cm^2. The thickness of the OP-GaP crystal was 500 μm with the QPM period 110 μm. The dispersion operator Re$[k(\omega)]$ includes all dispersion orders calculated from the refractive index given in ref. [61]. The nonlinear coefficient of GaP is $d_{14} = 35$ pm/V. As for the value of nonlinear refraction, we took $n_2 = 1.9 \times 10^{-18}$ m^2/W; this was based on the measured value ($n_2 = 7 \times 10^{-18}$ m^2/W) for λ=1.04 μm [26] scaled to λ≈4.7 μm using the scaling law derived from the two-band model of a

semiconductor [41]. The refractive index, group velocity, and group velocity dispersion of GaP is shown in Figure 21.

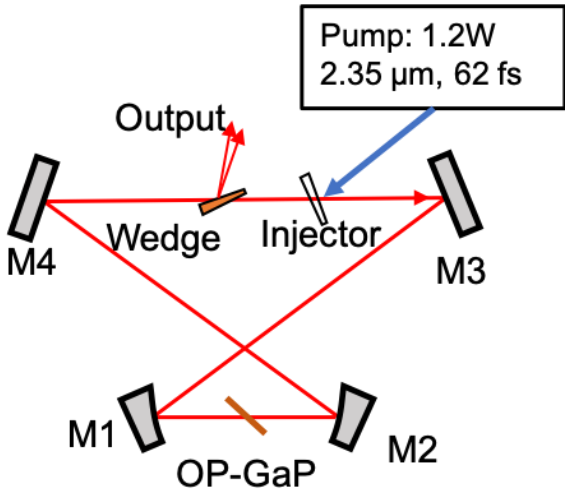

Figure 20. Schematic of OPO. The injector highly reflects the pump and highly transmits the signal and idler waves.

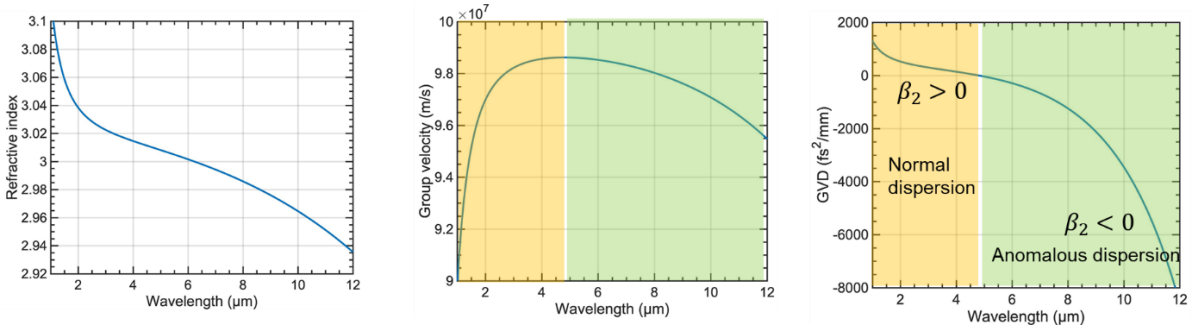

Figure 21. Refractive index (left), group velocity (middle), group velocity dispersion (right) of GaP in the MIR.

Output Spectrum

Figure 22(a) shows the injector transmittance and normalized parametric gain (acceptance bandwidth) calculated from a phase-mismatch to the pump. The injector has a broad transparency from 3 μm to 12 μm and a high reflection for the pump pulse. Figure 22(b) shows the calculated extra phase for each element and their total [62]. The total extra phase has a broad flat region, where the pump and the generated signal propagate at the same group velocity. The asterisks indicate the spectral point where the acquired phase per roundtrip is multiplication of 2π compared to the flat phase portion of OPO. The simulated spectrum agrees well with experimental data as shown in Figure 22(c). In addition to OPO spectrum, the broadening of pump pulse and the oscillatory behavior of SFG due to the drastic phase accumulation corresponds well with the experiment.

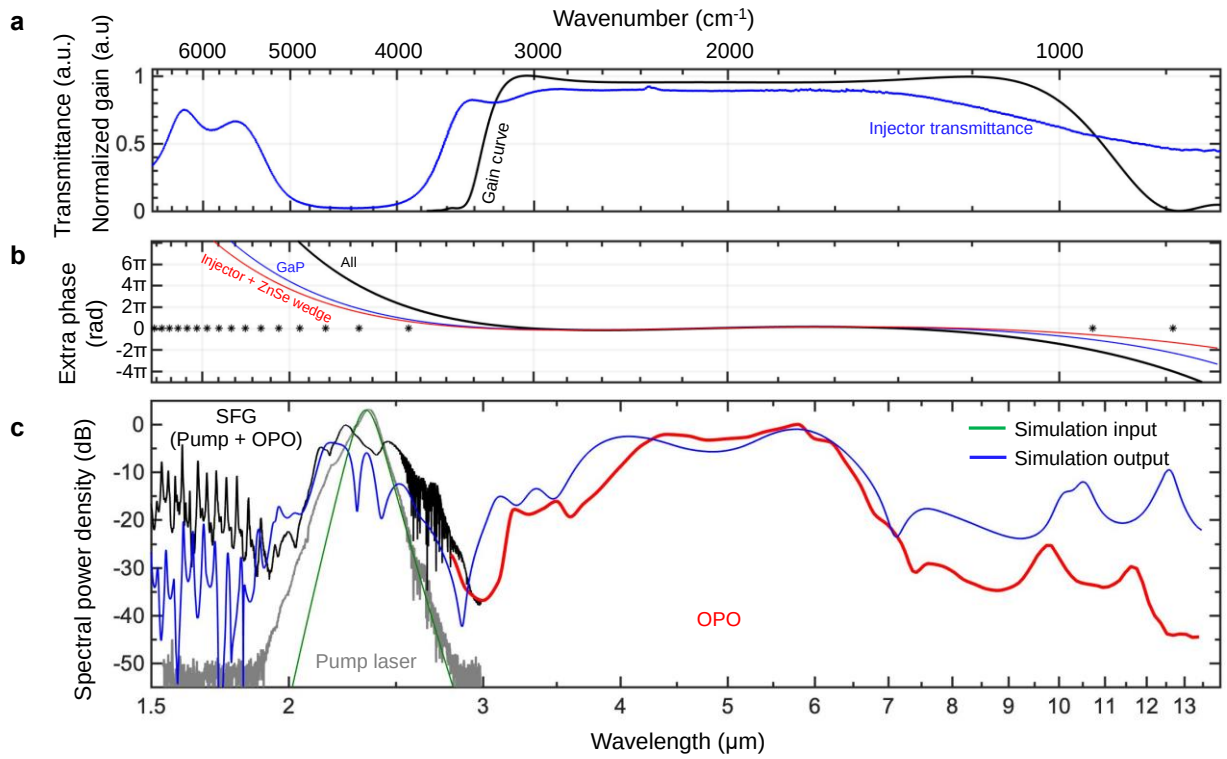

Figure 22. (a) The injector transmission and the normalized parametric gain. (b) Calculated extra phase in a cavity for each optical component. (c) The output spectrum of the experiment (red) and the simulation (blue).

Figure 23 presents the color-coded intensity spectrum as a function of cavity length detuning for the experiment (left), the simulation that includes all possible instantaneous three- and four-wave interactions (middle) and the simulation that includes only three-wave interactions (right). First, the calculated spectrum matches well with the experimental spectrum if taking into the account of $\chi^{(3)}$. The role of $\chi^{(3)}$ is (i) smoothening the long-wave spectrum around 7-10 μm and (ii) filling the dip at the degenerate wavelength at 4.7 μm. In the non-degenerate mode, one can

see that spectrum in the signal is broader than that of idler, which is not the case for only with $\chi^{(2)}$ where you split one photon into two. This can be explained by the fact that the SPM induced spectral broadening is proportional to the photon energy. Also, SPM effects in the normal dispersion regime can generate new high/low frequencies, on the other hand in the anomalous dispersion regime, SPM compensates pulse broadening and leads soliton-like propagation. Another $\chi^{(3)}$ effect to be mentioned here is four-wave mixing (FWM). In the long-wavelength portion of OPO spectrum, the phase-matching condition is satisfied thanks to the anomalous dispersion in GaP. For example, in the degenerate case, the 2 photons at 6 μm transfer to 4.5 μm and 11 μm.

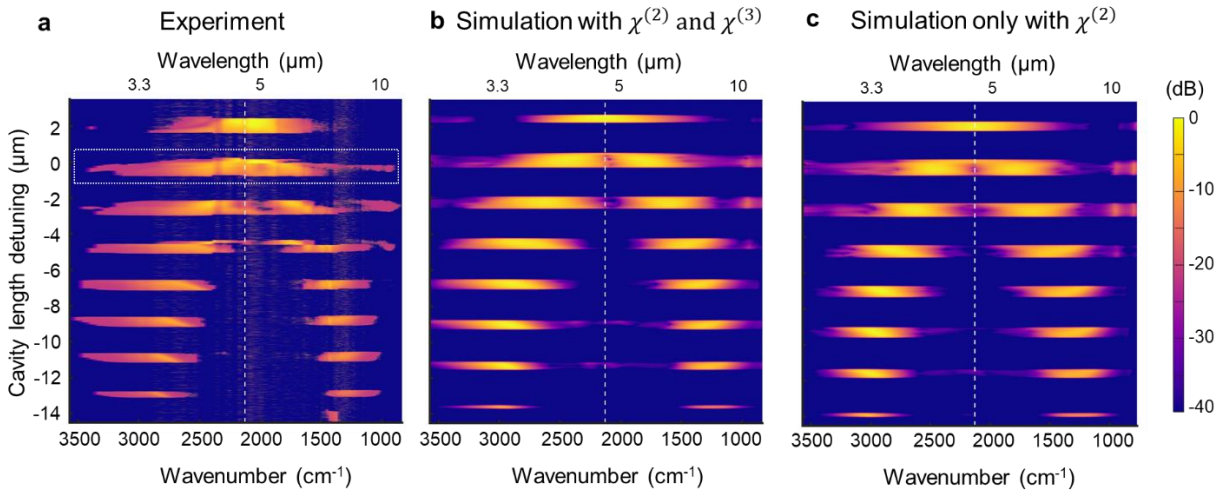

Figure 23. Spectrum vs. cavity length detuning. Experimental spectrum (left), simulated spectrum with both $\chi^{(2)}$ and $\chi^{(3)}$ included (middle), simulated spectrum with only $\chi^{(2)}$ (right).

The single wave method also covers the SH range of the pump laser. Some peaks of SH can be explained by the process of high order quasi-phase matching. Since the QPM grating has many different frequency components, the phase matching can occur for unexpected wavelengths. The phase-mismatch for higher order in SHG is expressed as follow

$$\Delta k_{\mathrm{SHG}} = n_2 \frac{2\pi}{\lambda_2} - 2n_1 \frac{2\pi}{\lambda_1} - (2m+1)\frac{2\pi}{\Lambda} \qquad (16)$$

where m indicates the m^{th}-order QPM grating and Λ is the period of OP-GaP. It is noted, however, that the efficiency of m^{th}-order phase-matching is proportional to $(2m+1)^{-2}$. Figure 24 shows the simulated and experimental spectrum in 700-1800 nm range when OPO is operating and when OPO is not operating. The high-order QPM curve predicts the peak in SHG, and it matches well with the experiment. The higher order of m = 2,3 is observed. This calculation results can be helpful when detecting the carrier envelope offset frequency at near infrared region.

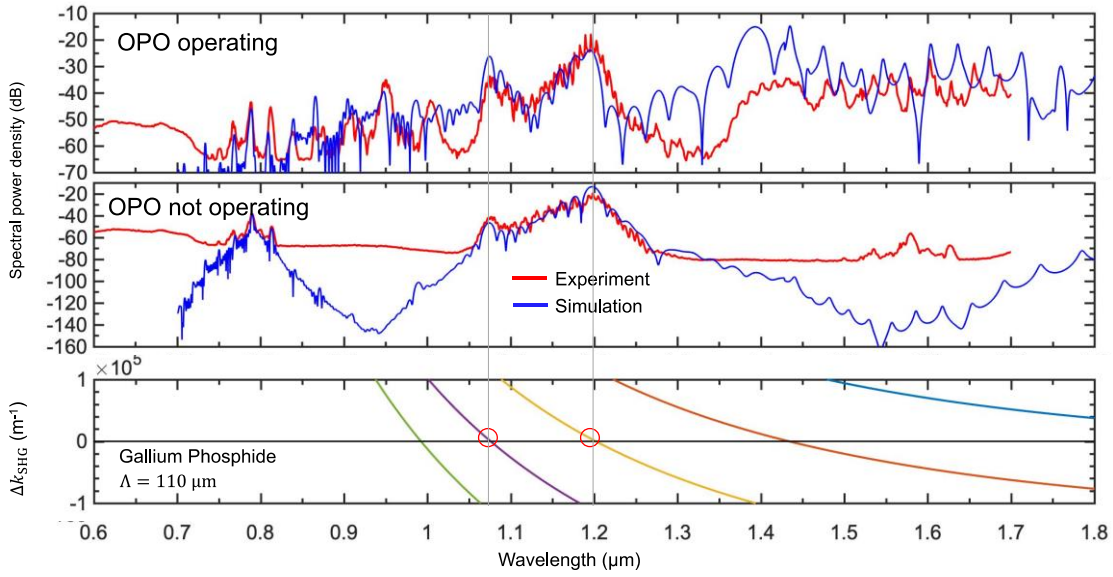

Figure 24. Simulated output spectrum in 700-1800 nm. The bottom figure shows the high-order (m = 0, 1, 2, 3, 4 from right to left) QPM phase mis-matching curve for SHG.

In subharmonic OPO the large pump depletion has been observed. The simulation tracks the energy transfer of the pump. As Figure 25 shows that for the small output-coupling (3.4%) the pump deletion is found to be 68% and most of the pump power amplifies (compensating the loss) the mid-infrared pulse. Some other energy transfers to SFG and SHG. The circulating mid-infrared pulse has 1.6 times higher energy than that of the pump energy (100 vs. 157 in Figure 25). The average output power is calculated to be 64 mW, which is a good agreement with the value 53 mW obtained in the experiment.

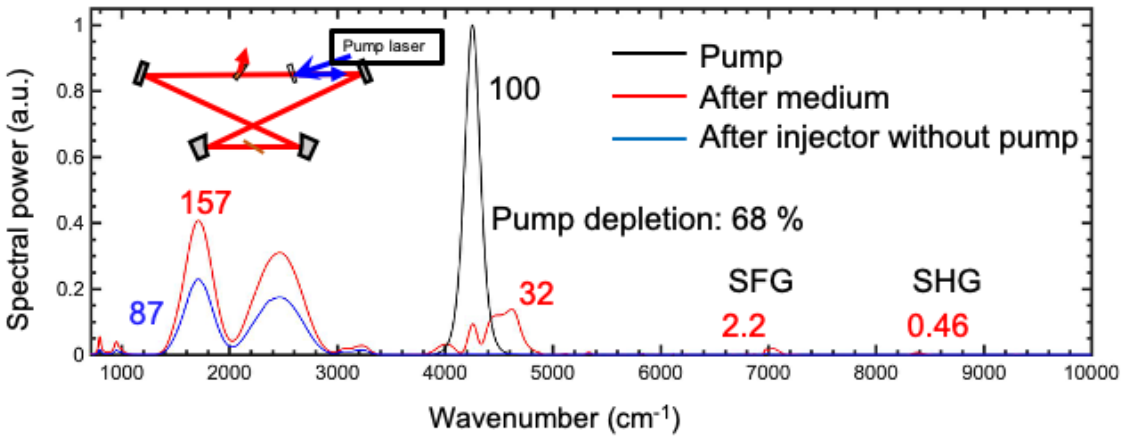

Figure 25. The calculated energy conservation in the OPO. In a steady state of OPO, 68% of the newly injected pulse energy mostly converts to MIR energy.

Temporal Waveform

The equation directly solves the dynamics of the *E*-field of laser pulse in nonlinear medium, which contains the information about the phase. The *E*-field of MIR output is calculated after filtering out the MIR portion of 3-13 μm. Compared to the pulse duration of the pump pulse that is 62 fs, the OPO pulse duration is about 3 times shorter due to the broadened spectrum as shown in Figure 26. Also, the absolute peak amplitude of the *E*-filed is 2 times larger than the pump pulse.

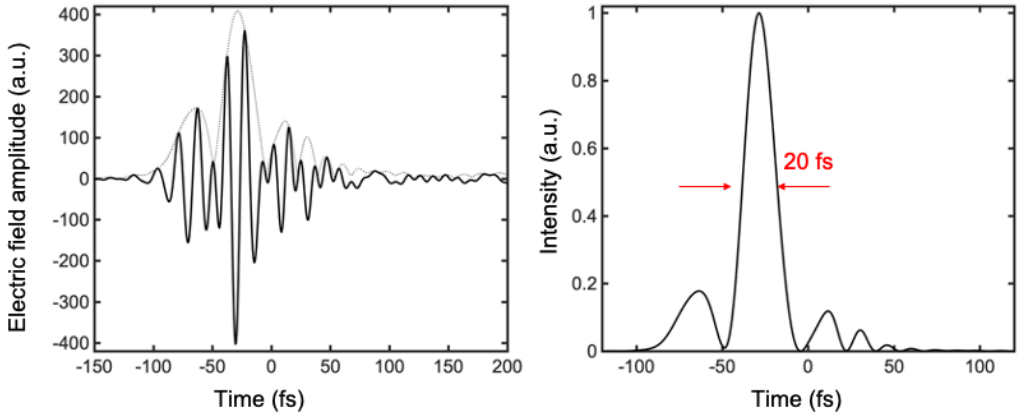

Figure 26. Simulated time-domain profiles for the *E*-field (left) and intensity (right) of the OPO pulse.

Regarding the top spectral band in Figure 23 that has a narrower spectrum than the second spectral band from the top, the pulse duration is 35 fs. This peak is relatively stable: less change of temporal and spectrum shape at every roundtrip. Also, the carrier envelope phase is analyzed briefly in time domain. Looking at the pulse train, as shown in Figure 27, the carrier phase of each pulse from a cavity is flipped exactly by π, indicating that the change of carrier phase is $\Delta\phi_{\mathrm{CEP}} = \pi$.

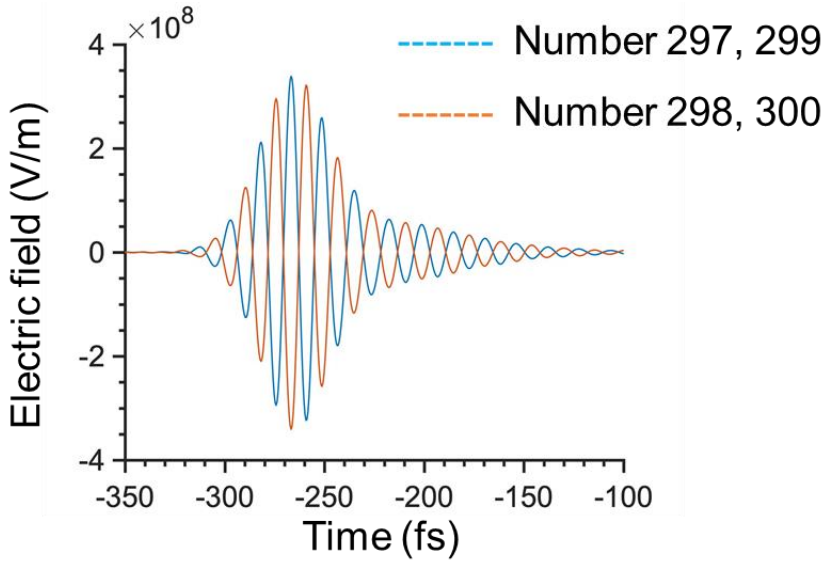

Figure 27. The electric fields for different number of trips in a cavity for the longest cavity length.

On the other hand, when it comes to the broadest spectral band (second peak from the top in Figure 23), every pulse is identical, indicating $\Delta\phi_{\mathrm{CEP}} = 0$. This is consistent with the parameter of CEO that is set to zero and thus the properties of phase in OPO. Additionally, it satisfies the property of phase-locking in subharmonic OPOs [53].

The pulse formation dynamics is also explored. So-called temporal simulton [63] is observed for the first peak from the top in Figure 23, which has a relatively higher threshold with larger conversion efficiency slope against input power. For the cavity length slightly longer than the synchronously operated cavity length, the pulse can accelerate in time to compensate the cavity length mismatch. Figure 28 agrees well with this theory where after a gain saturation, the pulse accelerates in time. This spectral band has the largest threshold among all other spectral bands, also indicating it is the simulton working regime.

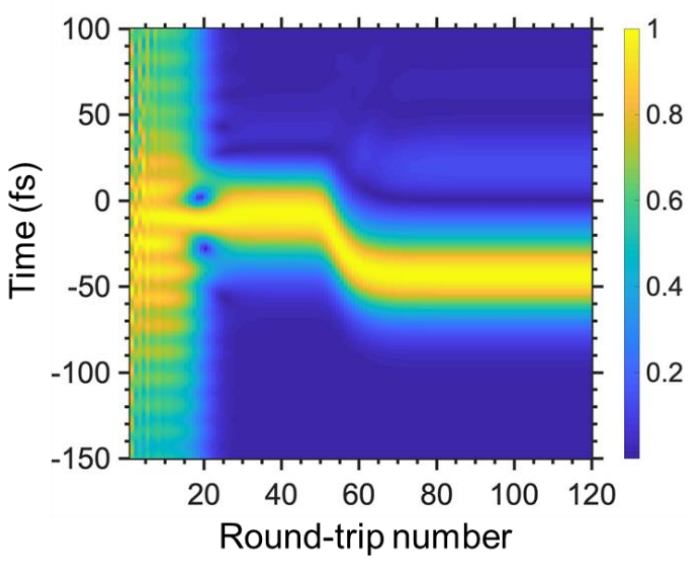

Figure 28. Pulse evolution for the longest cavity length. The envelope of electric field is normalized for each cavity round trip.

The simulation can be further extended to (i) calculate the spectrogram to visualize the time-dependent frequency within the pulse as a frequency resolved optical gating trace and (ii) analyze the stability of carrier envelope phase for each OPO output pulse.

CHAPTER FIVE: NONLINEAR ABSORPTION AND REFRACTION IN THE MID-INFRARED

Introduction

Nonlinear optical (NLO) materials have advanced coherent laser sources and applications such as frequency-comb spectroscopy for the mid-infrared (MIR) region. The exploration of such a coherent beam based on nonlinear frequency conversion via $\chi^{(2)}$ media is particularly active in recent years, and the large portion of MIR spectrum is covered limited only by the materials' transparency range. The broadband MIR generation has been achieved as frequency down-conversion in intra-pulse difference frequency generation based on GaP, ZnSe, GaSe, and ZGP [8–10,25], and in optical parametric oscillators based on GaP [15,64]. These crystals have an extremely broad MIR transparency stretching beyond 10 μm and possess high quadratic nonlinearity. Thanks to the crystals' relatively large band gap energies (> 2 eV), they are not expected to suffer from two-photon absorption when pumped at $\lambda > 1.25$ μm; however, with increasing available pump power by using e.g. few-cycle optical pulses, high-order effects may come into play even though MIR photon energy is small (~0.5 eV). To avoid roll-off of generated signal, high power laser sources require NLO materials with low multiphoton absorption (MPA). Accurately characterizing MPA will pave its way for more applications in high power sources in the MIR region. So far, among those crystals, there is no MPA ($N \geq 4$) measurement data available except four-photon absorption in GaP [21]. Another important mechanism contributing to nonlinear absorption (NLA) is free carrier absorption (FCA), which is led by MPA-assisted excited-state intraband absorption. The number of carriers generated is dependent on the pulse

duration, hence the pulse duration is the critical factor to assess FCA. In many NLA measurements, the effect of FCA is dismissed, leading to an overestimation of MPA.

The high-intensity pump pulses may introduce complex light-matter interactions beyond the conventional $\chi^{(2)}$ effect in these crystals due to the $\chi^{(3)}$ (or nonlinear refractive index n_2) effect such as self-focusing, self-phase modulation (SPM), and four-wave mixing. Such applications using n_2 effect include Kerr frequency comb in integrated photonics based on GaP [27,28] and supercontinuum generations based on ZnSe or GaSe [31,65]. The nonlinear refraction associated with spatial, spectral, and temporal effect needs to be characterized at the MIR for the nonlinear pulse evolution studies.

Experiment Setup

Figure 29 shows the schematic diagram of the experimental setup. We characterized the materials using nonlinear transmittance technique: open- (OA) and closed-aperture (CA) Z-scan. The beam of a linearly polarized mode-locked 2.35 μm Cr^{2+}:ZnS laser, with an average output power of 1.2 W, at 79 MHz repetition rate and 62-fs pulse duration was focused by an off-axis parabolic mirror (OAP), and the transmitted power was recorded while the sample was translated along the focus by a motorized stage. The material was placed closed to the normal incidence avoiding back reflection to the laser (ZGP was anti-reflection coated). The thickness of the materials was 0.50 mm for GaP, 0.10 mm for ZnSe, 0.46 mm for GaSe, and 1.0 mm for ZGP. The transmitted signal was measured using a large area pyroelectric detector. The input intensity was controlled by a variable neutral density filter (2-mm SiO_2 substrate) and was monitored by a reference detector to calibrate the transmitted power through the sample. With the knife-edge

measurement, the beam waist ($1/e^2$ in intensity) was found to be 8.5 μm for f = 15 mm OAP and 12 μm for f = 25 mm OAP, with the beam quality factor M^2 close to unity as shown in Figure 30.

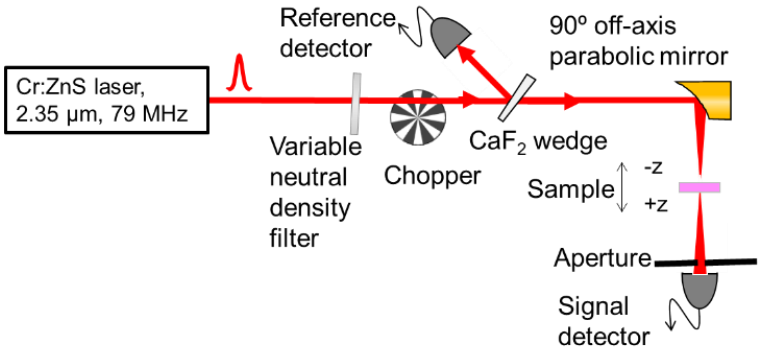

Figure 29. Experiment setup. The focal length of the OAP is f = 15 mm (only for CA Z-scan measurements f = 25 mm OAP was used). The aperture was used for CA Z-scan. The spectrum analyzer was used in the spectral broadening experiment.

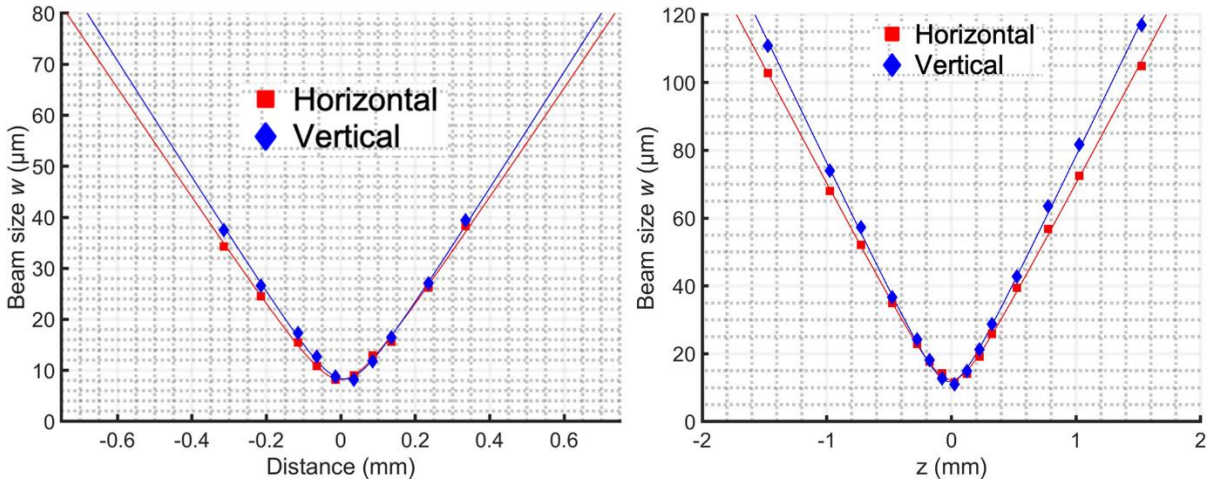

Figure 30. Beam profiles focused by f = 15 mm (left) and f = 25 mm (right) off-axis parabolic mirror.

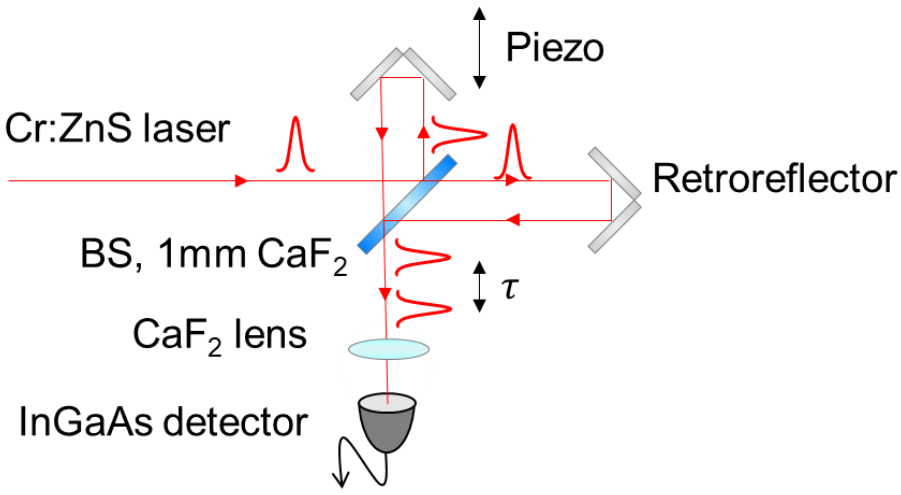

Figure 31. Interferometric autocorrelation based on two-photon absorption

The n_2 was also characterized in the frequency domain using the optical spectrum analyzer (OSA) by measuring the spectral broadening via SPM.

While multiphoton absorption is instantaneous process since the free carrier concentration accumulates in time, the pulse with longer duration has larger free carrier absorption when the peak intensities are same (Figure 32(a)). Note that their magnitude of MPA is the same. Therefore, to observe a FCA contribution, we stretched the pulse in time through dispersive material (a few mm sapphire plate) and measured pulse duration by intensity autocorrelation method, as shown in Figure 31 and Figure 32(b). Here, we used a different Cr^{2+}:ZnS laser with 30-fs pulse duration. With 2mm and 3mm sapphire windows, the pulse was stretched to 49 fs and 70 fs from 30 fs, respectively.

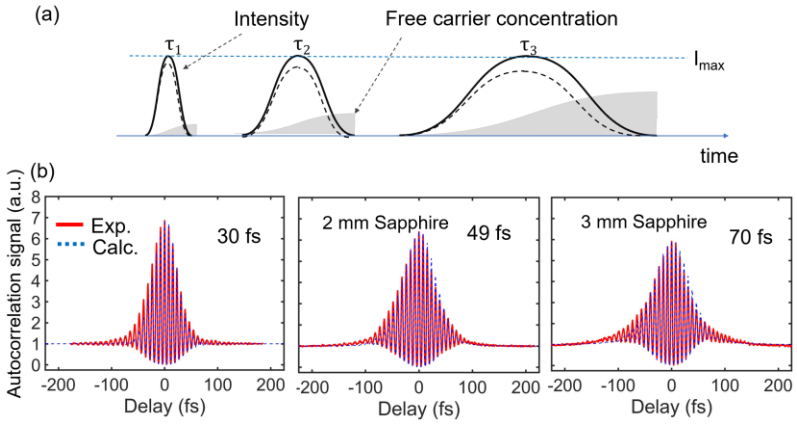

Figure 32. (a) Schematic of contribution of FCA depending on pulse duration. The dashed lines show intensities after FCA. (b) Pulse durations measured by autocorrelation measurements. The experimental trace was fitted with a numerical simulation considering the group velocity dispersion effect introduced by a sapphire plate.

Theoretical Modeling

The intensity changes along the propagation direction, followed by subsequent FCA can be modeled in Eq. (17,18) assuming the pulse does not 'see' the carriers created by previous pulses which have not yet recombined. According to the literature, the free carrier lifetime is an order of a few ns, which is shorter than our pulse train period [66–68].

$$\frac{dI}{dz} = -\alpha_N I^N - \sigma_c n_c I \qquad (17)$$

$$\frac{dn_c}{dt} = \frac{\alpha_N I^N}{N\hbar\omega} \qquad (18)$$

In terms of *E*-field, the pulse propagation inside a nonlinear material is modeled [69]

$$\frac{\partial \mathcal{E}(r,t,z)}{\partial z} = \frac{i}{2k}\Delta_\perp \mathcal{E}(r,t,z) - \frac{\alpha_N}{2} I^{(N-1)} \mathcal{E}(r,t,z) + i\frac{\omega}{c} n_2 I \mathcal{E}(r,t,z) \qquad (19)$$

n_c is the density of free carriers excited by MPA and σ_c is the FCA cross section. $\mathcal{E}(r,t,z)$ is the complex electric field amplitude, k is the wavenumber, $\Delta_\perp$ is the transverse Laplacian operator, α_N is the N^{th} order MPA coefficient, and I is the intensity expressed as $I = \epsilon_0 cn|\mathcal{E}|^2/2$. For modeling CA Z-scan experiment, the propagation to an aperture after a nonlinear material was modeled by Fresnel diffraction integral. The numerical implementation was done with the Crank-Nicolson algorithm to account the diffraction term and the nonlinearity was treated by the second-order Adams-Bashforth scheme. The diffraction term is required for characterizing samples beyond thin sample approximation. The nonlinear transmittance was calculated by temporally and spatially integrating the pulse energy after the propagation.

FCA term is integrated into the equation as $-\frac{\sigma_c}{2}\frac{\alpha_N}{N\hbar\omega}\int_{-\infty}^{t} I^N(t')\,dt'\,\mathcal{E}(r,t,z)$ and similarly solved with the numerical method. The carrier density is also distributed corresponding to the intensity profile. The equations show that the FCA term is the order (*N+1*), implying FCA will dominate NLA as the intensity becomes high.

Multiphoton Absorption Results

To determine the dominant MPA order *N*, we performed OA Z-scan in a small absorption ($|\Delta T|$<1%, where *T* is the transmission) regime, where -ΔT is proportional to the intensity to the power (*N*-1). Figure 33 is the *log-log* overview plot of the transmission change vs. peak intensity for different crystals. The value of the linear fitting slope is summarized in Table 2 with the good accordance with the expected MPA order *N* from the corresponding direct band-gap energies

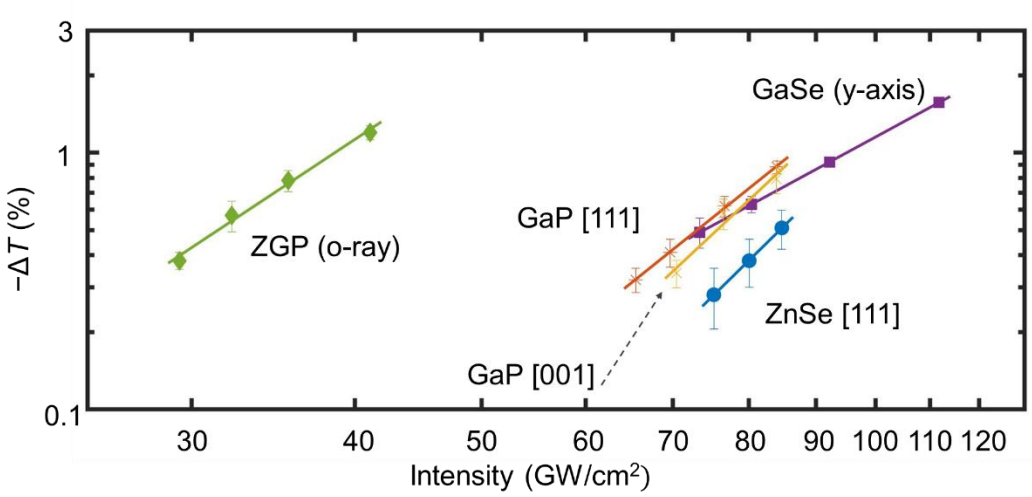

Figure 33. The transmission change vs. the on-axis peak intensity for the different crystals.

To compare these samples on the same page by normalizing by their thickness, we calculated the required peak intensity to have nonlinear absorption of 1 cm^{-1}. We found that GaSe can tolerate the most to NLA while ZGP suffers from the absorption loss the most.

Table 2. Experimentally obtained MPA order and the tolerance of nonlinear absorption for different crystals.

	GaP	ZnSe	GaSe	ZGP
Thickness (mm)	0.50	0.10	0.46	1.0
Theoretical MPA order *N*	6	5-6	4	4
Experiment *N*	6.6 [111] 5.6 [110] 7.5 [001] Ave. 6.6	4.9 [111] 4.8 [110] 4.6 [001] Ave. 4.8	3.9 (x-axis) 3.9 (y-axis) Ave. 3.9	4.1 (o-ray) 4.7 (e-ray) Ave. 4.4
Peak intensity (GW/cm^2) required for NL absorption of 1 cm^{-1}	100	95	143	52

Figure 34 shows the nonlinear transmission at $|\Delta T|>1\%$. A linear slope was observed for the materials. This is because at higher intensities the contribution of FCA becomes larger, or the self-focusing brings more absorption by increasing the intensity inside a material. It is expected that the absorption will be saturated as increasing the intensity by power depletion, especially for these high-order MPAs. GaP showed different slopes for different crystal orientations, but on average it follows the theoretically predicted value based on the band bap energy. ZnSe has a direct band bap energy of 2.7 eV, which corresponds to a cut-off wavelength of 2300 nm for 5 photon absorption. The pump laser has a broad spectrum and contains 21% of total energy below 2300 nm, which can lead to 5 photon absorption. GaSe and ZGP have the same magnitude of band gap energy and show 4 photons are involved in MPA, however, ZGP showed slightly higher slope.

The fluorescence was observed due to the recombination of upper state carrier excited by MPA. Corresponding to crystals' band gap energy, ZnSe had blue light emission and GaSe had red light emission. Although GaP has larger direct band gap energy than that of ZnSe, the fluorescence from GaP was green light emission, indicating the recombination happens in an indirect band gap (2.26 eV) assisted by phonon.

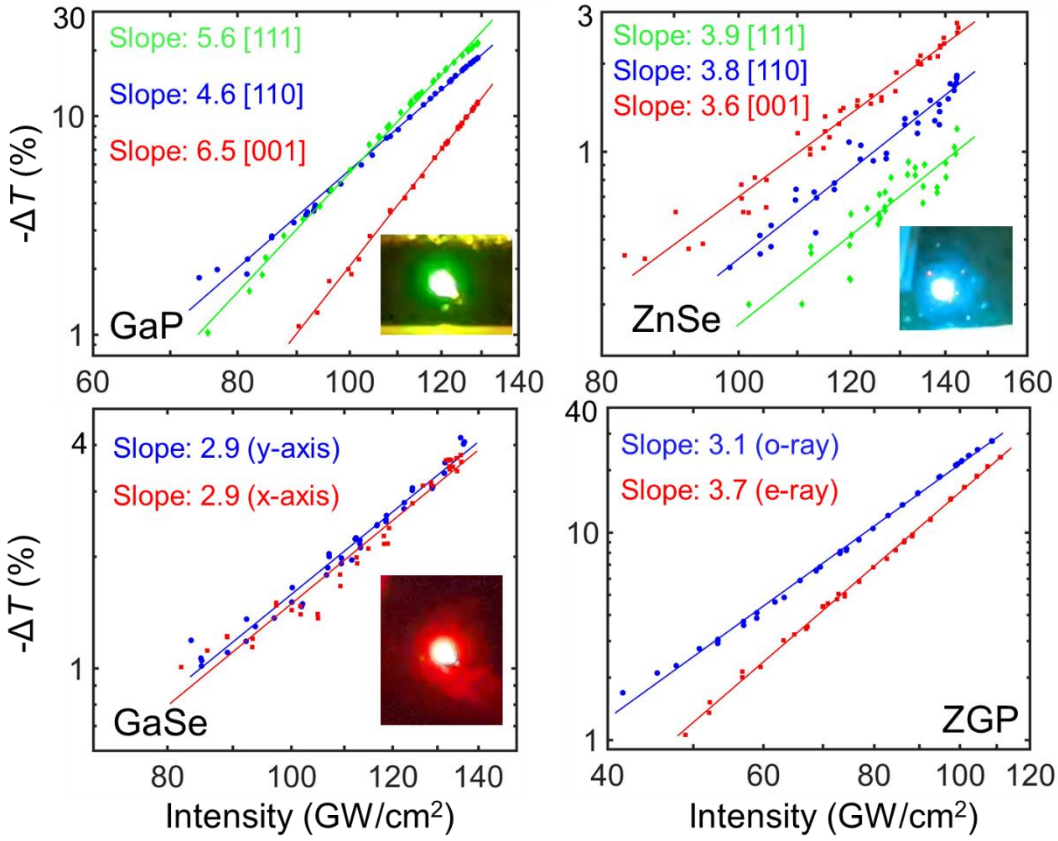

Figure 34. The transmission change vs. the on-axis peak intensity for the different crystals at higher intensities. Insets show fluorescence from the crystals.

For GaP we performed OA Z-scan measurement in two regions with different crystal growth, substrate and orientation patterned portion, and there was no difference observed for NLA.

Free Carrier Absorption Results

Because free carriers accumulate over the length of excitation pulse, FCA is expected to be a function of pulse duration at fixed peak intensity. To estimate the role of free carriers, we performed the OA Z-scan for different pulse durations, while we controlled the intensity by the neutral density filter to keep the peak intensity for the pulses of different durations at the same level. Assuming that at the shortest pulse duration of 30 fs the FCA is neglected, we fitted experimental results by letting the absorption cross section σ_c as a variable. The peak intensity of 110 GW/cm^2 was used for GaP and ZGP, and that of 220 GW/cm^2 was used for ZnSe and GaSe. For ZnSe and GaSe, nonlinear absorption was measured only at two different pulse durations due to their relatively small total NLAs compared to GaP and ZGP. Figure 35 shows the numerical simulation with the experiment result (marked as a green star) of how NLA changes with different pulse duration in GaSe. Here we assumed the MPA to be 2%, and used σ_c as a fitting parameter. As expected, when there are no FCA, the total NLA does not change with the input pulse duration. Also, the effect of FCA becomes larger for the larger free carrier cross section.

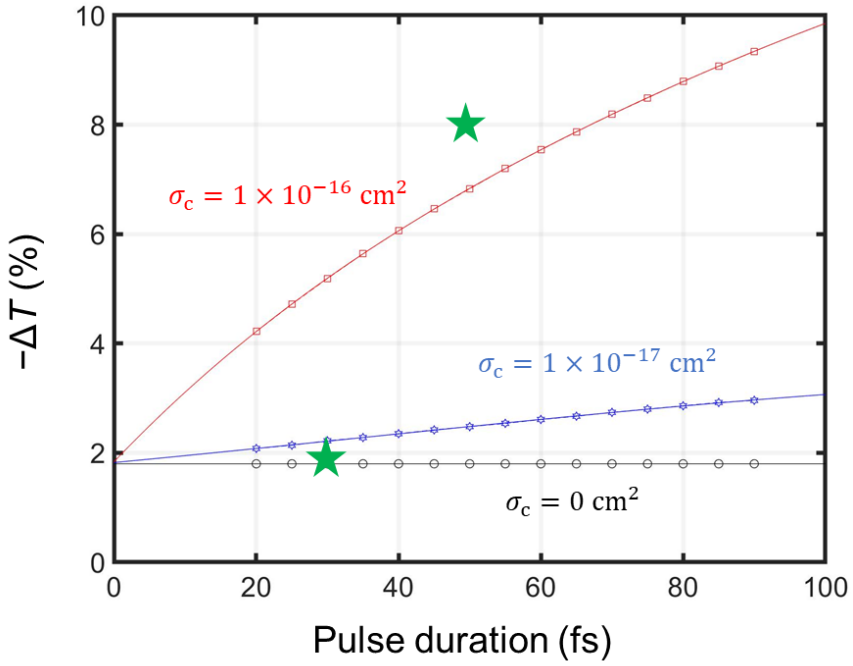

Figure 35. Numerical simulation of NLA with different pulse durations for a fixed MPA in GaSe. The points show the numerically calculated NLA at a fixed pulse duration, and the lines are the fitting for a constant FCA cross section. The stars show experiment result at the pulse durations of 30 and 49 fs.

Table 3 shows our experimental results for the total NLA vs. pulse duration at a constant peak intensity and extracted FCA cross sections. We found that NLA strongly depends on pulse duration, even for the shortest pulses, the contribution of FCA can be significant and comparable to that of MPA, which is usually dismissed and leads to overestimating of MPA coefficients. The extracted FCA cross sections, ranging from $2\text{x}10^{-15}$ to $2\text{x}10^{-16}$ cm^2, are 10 to 20 times larger than those reported in literature [70–72], considering the wavelength dependence. A possible explanation for this mismatch is that a constant FCA cross section model, valid for low levels of irradiation, is no longer valid at our peak intensities (> 100 GW/cm^2) and peak *E*-fields (> 5

MV/cm). Different high-field effects in the conduction band may occur, such as multi-photon absorption to higher lying bands, or even scattering to adjacent valleys of the conduction band.

Table 3. Nonlinear absorption for different input pulse durations and obtained FCA cross section.

Nonlinear absorption (%)	GaP [111]	ZnSe [111]	GaSe (y-axis)	ZGP (o-ray)
Pulse duration 30 fs	1%	1%	2%	5%
Pulse duration 49 fs	2%	3%	8%	30%
Pulse duration 70 fs	12%	N/A	N/A	37%
FCA cross section σ_c (cm^2)	$2x10^{-15}$	$5x10^{-16}$	$2x10^{-16}$	$2x10^{-15}$

Nonlinear Refractive Index Results.

The nonlinear refractive index n_2 was characterized via two methods: CA Z-scan technique and spectral broadening method. The value of n_2 obtained is summarized in Table 4.

In CA Z-scan experiment, the peak intensity was reduced so that there was no NLA, which is around 20 GW/cm^2 for ZGP and 70 GW/cm^2 for the other three crystals. The experimental data were fitted with the modeling and the n_2 was determined. The linear transmittance at the aperture was around 6%. Figure 36 shows the experimental data and the numerical fitting for different

crystals, including 0.5-mm poly-ZnSe. We first measured ZnSe as a reference sample whose n_2 is well studied to validate our CA Z-scan method.

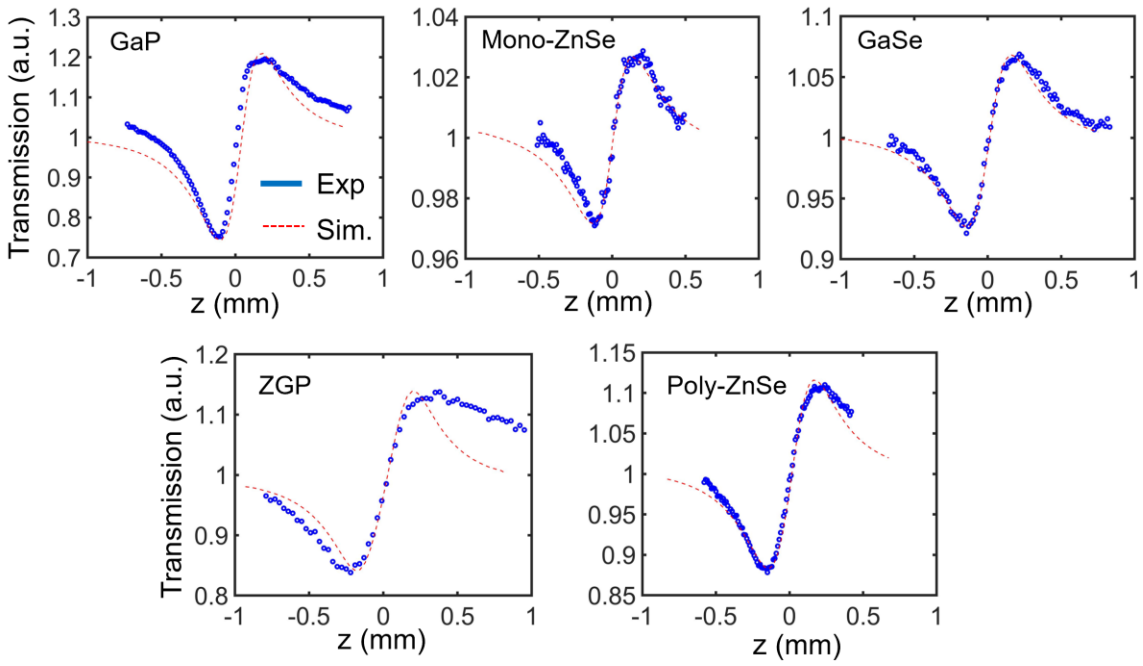

Figure 36. CA Z-scan curves for different crystals. The dashed curves are the fittings from the model.

GaP had the highest n_2 and GaSe had the lowest n_2 among these crystals, which did not follow the dependence of $n_0^{-2}E_g^{-4}$ derived from the two-band model of a semiconductor [41]. For mono- and poly-ZnSe we got almost the same value.

We also characterized n_2 value through spectral broadening experiment. The sample was set at the focus and the output spectrum was recorded through an OSA. Only the central portion of the beam was coupled into the OSA. The spectral broadening by SPM was evaluated by the model including the total absorption, where GaP, GaSe, ZGP, and poly-ZnSe had the absorption of 25%, 4%, 48%, and 13%, correspondingly, with the intensity inside the materials around 150

GW/cm^2. For mono-ZnSe no spectral broadening was observed due to the smaller thickness. The original spectrum and the broadened spectrum with the fitting are shown in Figure 37. In ZGP the spectrum bandwidth (FWHM) was broadened from 96 nm to 148 nm.

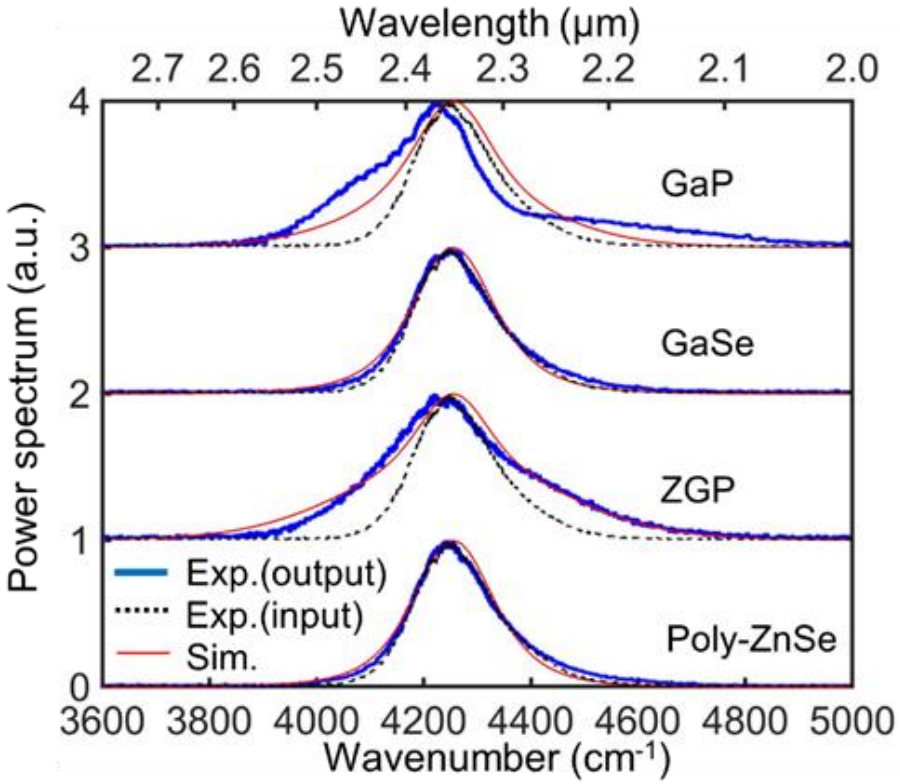

Figure 37. Spectral broadening via self-phase modulation.

Comparing with the values obtained from the CA Z-scan, they have a good match in terms of their order of magnitude among the crystals (Table 4).

Table 4. Measured values of n_2 for different crystal in the CA Z-scan method and spectral broadening method.

n_2 (10^{-18} m^2/W)	GaP [111]	Mono-ZnSe [111]	GaSe (y-axis)	ZGP (o-ray)	Poly-ZnSe
CA Z-scan	1.8	1.0	0.62	1.7	0.88
Spectral broadening	1.8	N/A	0.80	1.7	1.1
n_2 from literature	3.5 [28] 1.9 [21]	1.1 [73]	2.1 [23]	5.3 [74]	1.2 [31] 1.2 [23]

Comparing n_2 with other literature, that of GaP and ZnSe has a good match, however, the one for GaSe and ZGP is 3 times smaller than those reported.

CHAPTER SIX: CONCLUSIONS

Nonlinear optical frequency conversion is a powerful technique to generate MIR wavelength preserving a coherence of the pump laser. Through the use of high peak power MIR laser system or a few cycle pulses, various nonlinear interactions were studied both theoretically and experimentally, such as RPM, a combination of second- and third-order nonlinearity in OPO, nonlinear absorption, and nonlinear refraction.

A rigorous model for RPM in a cubic zinc-blende structure was developed, which is based on the local nonlinear susceptibility distribution and the real grain size distribution. The model verified the statistical SHG distribution result obtained in our experiment. The theory of RPM where the power grows linearly with material thickness was confirmed. The output polarization state was found to become random as a beam propagate long distance in the medium. It was also shown that in the case of ultrafast interactions with focused beams, a disordered material consisting of randomly oriented domains can perform on par with a QPM material, and the world's first OPO based on a disordered $\chi^{(2)}$ material was demonstrated. RPM in polycrystalline materials, in addition to polycrystalline ZnSe, opens a new route for ultrafast interactions, for frequency up and down conversion, as well as for producing ultra-broadband mid-infrared frequency combs via frequency division.

A numerical wave-propagation model for OP-GaP based ultra-broadband MIR OPO was presented. Using a nonlinear single-wave propagation model, the evolution of MIR pulse inside the cavity was characterized in frequency and time domain by treating all interacting frequencies as a single field. The propagation model in OPO and the details of the numerical calculation were

presented. The result of spectral evolution matched well with the experimental results, supported by the analysis of the extra phase in the cavity. By turning on and off the effect of cubic nonlinearity in the simulation, it was found that the high intensity circulating pulse induced SPM or FWM to make the spectrum broad and smooth. The simulation also predicted the spectrum shape in the near infrared region where the shape aligned with the high-order QPM theory. In the time domain, the electric field of MIR pulse was derived as well as its intensity form. The pulse formation dynamics in OPO were also analyzed and supported the theoretical predictions.

High-order nonlinear optical effects in the MIR range were characterized for GaP, ZnSe, GaSe, and ZGP crystals. OA Z-scan measurements revealed the MPA order for each crystal, and it followed the predicted theoretical order derived from the bandgap energies. Out of the four crystals, GaSe had the least nonlinear absorption among all. Also, nonlinear absorption measurement with different pulse durations but with constant peak intensity revealed strong dependence on pulse duration due to accumulation of free carriers and their possibly strong nonlinear response at high irradiation field. The nonlinear refractive index for these crystals was obtained through the CA Z-scan method and spectral broadening experiment. With the numerical modeling, the values obtained from both experiments had a good match. These results will be critical parameters when designing experimental setups and analyzing a complex beam propagation inside nonlinear materials.

APPENDIX: COPYRIGHT PERMISSION

Dear Taiki Kawamori,

Thank you for contacting Optica Publishing Group.

For the use of material from Q. Ru, T. Kawamori, P. G. Schunemann, S. Vasilyev, S. B. Mirov, and K. L. Vodopyanov, "Two-octave-wide (3–12 μm) subharmonic produced in a minimally dispersive optical parametric oscillator cavity," Opt. Lett. 46, 709-712 (2021):

> Because you are the author of the source paper from which you wish to reproduce material, Optica Publishing Group considers your requested use of its copyrighted materials to be permissible within the author rights granted in the Copyright Transfer Agreement submitted by the requester on acceptance for publication of his/her manuscript. If the entire article is being included, it is requested that the **Author Accepted Manuscript** (or preprint) version be the version included within the thesis and that a complete citation of the original material be included in any publication. This permission assumes that the material was not reproduced from another source when published in the original publication.
>
> The **Author Accepted Manuscript** version is the preprint version of the article that was accepted for publication but not yet prepared and/or formatted by Optica Publishing Group or its vendors.

While your publisher should be able to provide additional guidance, we prefer the below citation formats:

> For citations in figure captions:
>
> [Reprinted/Adapted] with permission from [ref #] © Optica Publishing Group. (Please include the full citation in your reference list)
>
> For images without captions:
>
> Journal Vol. #, first page (year published) An example: Opt. Express 19, 2720 (2011)

Please let me know if you have any questions.

Kind Regards,
Hannah Greenwood

Hannah Greenwood
November 2, 2021
Authorized Agent, Optica Publishing Group

T. Kawamori, Q. Ru, and K. L. Vodopyanov, “Comprehensive model for randomly phase-matched frequency conversion in zinc-blende polycrystals and experimental results for ZnSe,” Phys. Rev. Appl. 11, 054015 (2019).

REFERENCES

1. A. Schliesser, N. Picqué, and T. W. Hänsch, "Mid-infrared frequency combs," Nature Photonics **6**, 440 (2012).

2. N. Picqué and T. W. Hänsch, "Frequency comb spectroscopy," Nature Photonics **13**, 146 (2019).

3. S. Vasilyev, V. Smolski, J. Peppers, I. Moskalev, M. Mirov, Y. Barnakov, S. Mirov, and V. Gapontsev, "Middle-IR frequency comb based on Cr:ZnS laser," Opt. Express **27**, 35079 (2019).

4. S. A. Meek, A. Poisson, G. Guelachvili, T. W. Hänsch, and N. Picqué, "Fourier transform spectroscopy around 3 μm with a broad difference frequency comb," Applied Physics B **114**, 573 (2014).

5. F. C. Cruz, D. L. Maser, T. Johnson, G. Ycas, A. Klose, F. R. Giorgetta, I. Coddington, and S. A. Diddams, "Mid-infrared optical frequency combs based on difference frequency generation for molecular spectroscopy," Opt. Express **23**, 26814 (2015).

6. K. F. Lee, C. J. Hensley, P. G. Schunemann, and M. E. Fermann, "Midinfrared frequency comb by difference frequency of erbium and thulium fiber lasers in orientation-patterned gallium phosphide," Opt. Express **25**, 17411 (2017).

7. I. Pupeza, D. Sánchez, J. Zhang, N. Lilienfein, M. Seidel, N. Karpowicz, T. Paasch-Colberg, I. Znakovskaya, M. Pescher, W. Schweinberger, V. Pervak, E. Fill, O. Pronin, Z. Wei, F.

Krausz, A. Apolonski, and J. Biegert, "High-power sub-two-cycle mid-infrared pulses at 100 MHz repetition rate," Nature Photonics **9**, 721 (2015).

8. S. Vasilyev, I. S. Moskalev, V. O. Smolski, J. M. Peppers, M. Mirov, A. v Muraviev, K. Zawilski, P. G. Schunemann, S. B. Mirov, K. L. Vodopyanov, and V. P. Gapontsev, "Super-octave longwave mid-infrared coherent transients produced by optical rectification of few-cycle 2.5-μm pulses," Optica **6**, 111 (2019).

9. J. Zhang, K. Fritsch, Q. Wang, F. Krausz, K. F. Mak, and O. Pronin, "Intra-pulse difference-frequency generation of mid-infrared (2.7-20 μm) by random quasi-phase-matching," Opt. Lett. **44**, 2986 (2019).

10. Q. Wang, J. Zhang, A. Kessel, N. Nagl, V. Pervak, O. Pronin, and K. F. Mak, "Broadband mid-infrared coverage (2-17 μm) with few-cycle pulses via cascaded parametric processes," Opt. Lett. **44**, 2566 (2019).

11. F. Adler, K. C. Cossel, M. J. Thorpe, I. Hartl, M. E. Fermann, and J. Ye, "Phase-stabilized, 1.5 W frequency comb at 2.8-4.8 μm," Opt. Lett. **34**, 1330 (2009).

12. K. Iwakuni, G. Porat, T. Q. Bui, B. J. Bjork, S. B. Schoun, O. H. Heckl, M. E. Fermann, and J. Ye, "Phase-stabilized 100 mW frequency comb near 10 μm," Applied Physics B **124**, 128 (2018).

13. V. Smolski, S. Vasilyev, I. Moskalev, M. Mirov, Q. Ru, A. Muraviev, P. Schunemann, S. Mirov, V. Gapontsev, and K. Vodopyanov, "Half-Watt average power femtosecond source

spanning 3–8 μm based on subharmonic generation in GaAs," Applied Physics B **124**, 101 (2018).

14. Q. Ru, Z. E. Loparo, X. Zhang, S. Crystal, S. Vasu, P. G. Schunemann, and K. L. Vodopyanov, "Self-referenced octave-wide subharmonic GaP optical parametric oscillator centered at 3 μm and pumped by an Er-fiber laser," Opt. Lett. **42**, 4756 (2017).

15. Q. Ru, T. Kawamori, P. G. Schunemann, S. Vasilyev, S. B. Mirov, and K. L. Vodopyanov, "Two-octave-wide (3–12 μm) subharmonic produced in a minimally dispersive optical parametric oscillator cavity," Optics Letters **46**, 709 (2021).

16. N. Nagl, K. F. Mak, Q. Wang, V. Pervak, F. Krausz, and O. Pronin, "Efficient femtosecond mid-infrared generation based on a Cr:ZnS oscillator and step-index fluoride fibers," Opt. Lett. **44**, 2390 (2019).

17. H. Guo, C. Herkommer, A. Billat, D. Grassani, C. Zhang, M. H. P. Pfeiffer, W. Weng, C.-S. Brès, and T. J. Kippenberg, "Mid-infrared frequency comb via coherent dispersive wave generation in silicon nitride nanophotonic waveguides," Nature Photonics **12**, 330 (2018).

18. Q. Lu, D. Wu, S. Slivken, and M. Razeghi, "High efficiency quantum cascade laser frequency comb," Scientific Reports **7**, 43806 (2017).

19. B.-U. Sohn, C. Monmeyran, L. C. Kimerling, A. M. Agarwal, and D. T. H. Tan, "Kerr nonlinearity and multi-photon absorption in germanium at mid-infrared wavelengths," Applied Physics Letters **111**, 91902 (2017).

20. T. R. Ensley and N. K. Bambha, "Ultrafast nonlinear refraction measurements of infrared transmitting materials in the mid-wave infrared," Optics Express **27**, 37940 (2019).

21. B. Monoszlai, P. S. Nugraha, Gy. Tóth, Gy. Polónyi, L. Pálfalvi, L. Nasi, Z. Ollmann, E. J. Rohwer, G. Gäumann, J. Hebling, T. Feurer, and J. A. Fülöp, "Measurement of four-photon absorption in GaP and ZnTe semiconductors," Opt. Express **28**, 12352 (2020).

22. D. Haberberger, S. Tochitsky, and C. Joshi, "Fifteen terawatt picosecond CO2 laser system," Optics Express **18**, 17865 (2010).

23. J. J. Pigeon, D. A. Matteo, S. Ya. Tochitsky, I. Ben-Zvi, and C. Joshi, "Measurements of the nonlinear refractive index of $AgGaSe_2$, GaSe, and ZnSe at 10 μm," Journal of the Optical Society of America B **37**, 2076 (2020).

24. M. Rutkauskas, A. Srivastava, and D. T. Reid, "Supercontinuum generation in orientation-patterned gallium phosphide," Optica **7**, 172 (2020).

25. H. Timmers, A. Kowligy, A. Lind, F. C. Cruz, N. Nader, M. Silfies, G. Ycas, T. K. Allison, P. G. Schunemann, S. B. Papp, and S. A. Diddams, "Molecular fingerprinting with bright, broadband infrared frequency combs," Optica **5**, 727 (2018).

26. F. Liu, Y. Li, Q. Xing, L. Chai, M. Hu, C. Wang, Y. Deng, Q. Sun, and C. Wang, "Three-photon absorption and Kerr nonlinearity in undoped bulk GaP excited by a femtosecond laser at 1040 nm," Journal of Optics **12**, 095201 (2010).

27. D. J. Wilson, K. Schneider, S. Hönl, M. Anderson, Y. Baumgartner, L. Czornomaz, T. J. Kippenberg, and P. Seidler, "Integrated gallium phosphide nonlinear photonics," Nature Photonics **14**, 57 (2020).

28. A. Martin, S. Combrié, A. de Rossi, G. Beaudoin, I. Sagnes, and F. Raineri, "Nonlinear gallium phosphide nanoscale photonics [Invited]," Photonics Research **6**, B43 (2018).

29. Q. Ru, N. Lee, X. Chen, K. Zhong, G. Tsoy, M. Mirov, S. Vasilyev, S. B. Mirov, and K. L. Vodopyanov, "Optical parametric oscillation in a random polycrystalline medium," Optica **4**, 617 (2017).

30. S. Vasilyev, I. Moskalev, V. Smolski, J. Peppers, M. Mirov, V. Fedorov, D. Martyshkin, S. Mirov, and V. Gapontsev, "Octave-spanning Cr:ZnS femtosecond laser with intrinsic nonlinear interferometry," Optica **6**, 126 (2019).

31. K. Werner, M. G. Hastings, A. Schweinsberg, B. L. Wilmer, D. Austin, C. M. Wolfe, M. Kolesik, T. R. Ensley, L. Vanderhoef, A. Valenzuela, and E. Chowdhury, "Ultrafast mid-infrared high harmonic and supercontinuum generation with n2 characterization in zinc selenide," Opt. Express **27**, 2867 (2019).

32. C. K. N. Patel, "Optical harmonic generation in the infrared using a CO_2 laser," Phys. Rev. Lett. **16**, 613 (1966).

33. M. Baudrier-Raybaut, R. Haïdar, P. Kupecek, P. Lemasson, and E. Rosencher, "Random quasi-phase-matching in bulk polycrystalline isotropic nonlinear materials.," Nature **432**, 374 (2004).

34. S. Vasilyev, J. Gu, M. Mirov, Y. Barnakov, I. Moskalev, V. Smolski, J. Peppers, M. Kolesik, S. Mirov, and V. Gapontsev, "Low-threshold supercontinuum generation in polycrystalline media," Journal of the Optical Society of America B **38**, 1625 (2021).

35. R. Šuminas, A. Marcinkevičiūtė, G. Tamošauskas, and A. Dubietis, "Even and odd harmonics-enhanced supercontinuum generation in zinc-blende semiconductors," J. Opt. Soc. Am. B **36**, A22 (2019).

36. S. K. Kurtz and T. T. Perry, "A powder technique for the evaluation of nonlinear optical materials," J. Appl. Phys. **39**, 3798 (1968).

37. R. W. Boyd, *Nonlinear Optics*, 3rd ed. (Academic Press, 2008).

38. J. A. Armstrong, N. Bloembergen, J. Ducuing, and P. S. Pershan, "Interactions between light waves in a nonlinear dielectric," Phys. Rev. **127**, 1918 (1962).

39. T. Skauli, K. L. Vodopyanov, T. J. Pinguet, A. Schober, O. Levi, L. A. Eyres, M. M. Fejer, J. S. Harris, B. Gerard, L. Becouarn, E. Lallier, and G. Arisholm, "Measurement of the nonlinear coefficient of orientation-patterned GaAs and demonstration of highly efficient second-harmonic generation," Opt. Lett. **27**, 628 (2002).

40. M. Sheik-Bahae, A. A. Said, T. H. Wei, D. J. Hagan, and E. W. van Stryland, "Sensitive measurement of optical nonlinearities using a single beam," IEEE Journal of Quantum Electronics **26**, 760 (1990).

41. M. Sheik-Bahae, D. C. Hutchings, D. J. Hagan, and E. W. van Stryland, "Dispersion of bound electron nonlinear refraction in solids," IEEE Journal of Quantum Electronics **27**, 1296 (1991).

42. W. C. Hurlbut, Y.-S. Lee, K. L. Vodopyanov, P. S. Kuo, and M. M. Fejer, "Multiphoton absorption and nonlinear refraction of GaAs in the mid-infrared," Opt. Lett. **32**, 668 (2007).

43. M. D. Dvorak, W. A. Schroeder, D. R. Andersen, A. L. Smirl, and B. S. Wherrett, "Measurement of the anisotropy of two-photon absorption coefficients in zincblende semiconductors," IEEE Journal of Quantum Electronics **30**, 256 (1994).

44. D. C. Hutchings and B. S. Wherrett, "Theory of the anisotropy of ultrafast nonlinear refraction in zinc-blende semiconductors," Phys. Rev. B **52**, 8150 (1995).

45. S. Vasilyev, I. Moskalev, M. Mirov, S. Mirov, and V. Gapontsev, "Three optical cycle mid-IR Kerr-lens mode-locked polycrystalline Cr^{2+}:ZnS laser," Opt. Lett. **40**, 5054 (2015).

46. R. Šuminas, G. Tamošauskas, G. Valiulis, V. Jukna, A. Couairon, and A. Dubietis, "Multi-octave spanning nonlinear interactions induced by femtosecond filamentation in polycrystalline ZnSe," Appl. Phys. Lett. **110**, 241106 (2017).

47. E. Y. Morozov and A. S. Chirkin, "Stochastic quasi-phase matching in nonlinear-optical crystals with an irregular domain structure," Quantum Electronics **34**, 227 (2004).

48. X. Vidal and J. Martorell, "Generation of light in media with a random distribution of nonlinear domains," Physical Review Letters **97**, 1 (2006).

49. R. Kupfer, H. J. Quevedo, H. L. Smith, L. A. Lisi, G. Tiwari, C. G. Richmond, B. B. Bowers, L. Fang, and B. M. Hegelich, "Cascade random-quasi-phase-matched harmonic generation in polycrystalline ZnSe," J. Appl. Phys. **124**, 243102 (2018).

50. K. L. Vodopyanov, O. Levi, P. S. Kuo, T. J. Pinguet, J. S. Harris, M. M. Fejer, B. Gerard, L. Becouarn, and E. Lallier, "Optical parametric oscillation in quasi-phase-matched GaAs," Opt. Lett. **29**, 1912 (2004).

51. K. L. Vodopyanov, "Polarization-insensitive nonlinear-optical devices," Proc. SPIE **6875**, 68750 (2008).

52. R. Quey, P. R. Dawson, and F. Barbe, "Large-scale 3D random polycrystals for the finite element method: Generation, meshing and remeshing," Comput. Methods Appl. Mech. Eng. **200**, 1729 (2011).

53. A. Marandi, N. C. Leindecker, V. Pervak, R. L. Byer, and K. L. Vodopyanov, "Coherence properties of a broadband femtosecond mid-IR optical parametric oscillator operating at degeneracy," Optics Express **20**, 7255 (2012).

54. V. O. Smolski, H. Yang, S. D. Gorelov, P. G. Schunemann, and K. L. Vodopyanov, "Coherence properties of a 2.6–7.5 μm frequency comb produced as a subharmonic of a Tm-fiber laser," Optics Letters **41**, 1388 (2016).

55. Q. Ru, P. G. Schunemann, S. Vasilyev, S. B. Mirov, and K. L. Vodopyanov, "A 2.35-μm pumped subharmonic OPO reaches the spectral width of two octaves in the mid-IR," Conference on Lasers and Electro-Optics (CLEO), paper SF1H.1. (2019)

56. E. Gaižauskas, R. Grigonis, and V. Sirutkaitis, "Self- and cross-modulation effects in a synchronously pumped optical parametric oscillator," J. Opt. Soc. Am. B **19**, 2957 (2002).

57. H. Guo, X. Zeng, and M. Bache, "Generalized nonlinear wave equation in frequency domain," arXiv: 1301.1473 (2013).

58. T. Brabec and F. Krausz, "Nonlinear optical pulse propagation in the single-cycle regime," Physical Review Letters **78**, 3282 (1997).

59. M. Conforti, F. Baronio, and C. de Angelis, "Modeling of ultrabroadband and single-cycle phenomena in anisotropic quadratic crystals," J. Opt. Soc. of Am. B **28**, 1231 (2011).

60. H. Guo, X. Zeng, B. Zhou, and M. Bache, "Nonlinear wave equation in frequency domain: accurate modeling of ultrafast interaction in anisotropic nonlinear media," J. Opt. Soc. of Am. B **30**, 494 (2013).

61. J. Wei, J. M. Murray, J. O. Barnes, D. M. Krein, P. G. Schunemann, and S. Guha, "Temperature dependent Sellmeier equation for the refractive index of GaP," Optical Materials Express **8**, 485 (2018).

62. M. W. Haakestad, T. P. Lamour, N. Leindecker, A. Marandi, and K. L. Vodopyanov, "Intracavity trace molecular detection with a broadband mid-IR frequency comb source," J. Opt. Soc. of Am. B **30**, 631 (2013).

63. M. Jankowski, A. Marandi, C. R. Phillips, R. Hamerly, K. A. Ingold, R. L. Byer, and M. M. Fejer, "Temporal simultons in optical parametric oscillators," Physical Review Letters **120**, 053904 (2018).

64. L. Maidment, O. Kara, P. G. Schunemann, J. Piper, K. McEwan, and D. T. Reid, "Long-wave infrared generation from femtosecond and picosecond optical parametric oscillators based on orientation-patterned gallium phosphide," Applied Physics B **124**, 143 (2018).

65. S. Vasilyev, I. Moskalev, V. Smolski, J. Peppers, M. Mirov, A. Muraviev, K. Vodopyanov, S. Mirov, and V. Gapontsev, "Multi-octave visible to long-wave IR femtosecond continuum generated in Cr:ZnS-GaSe tandem," Optics Express **27**, 16405 (2019).

66. G. Lin, Q. Zhang, X. Lin, D. Zhao, R. Jia, N. Gao, Z. Zuo, X. Xu, and D. Liu, "Enhanced photoluminescence of gallium phosphide by surface plasmon resonances of metallic nanoparticles," RSC Advances **5**, 48275 (2015).

67. J. S. Weiner and P. Y. Yu, "Free carrier lifetime in semi-insulating GaAs from time-resolved band-to-band photoluminescence," Journal of Applied Physics **55**, 3889 (1984).

68. X. Zhang, S. Wang, G. Wan, Y. Zhang, M. Huang, and L. Yi, "Transient reflectivity measurement of photocarrier dynamics in GaSe thin films," Applied Physics B: Lasers and Optics **123**, 86 (2017).

69. A. Couairon, E. Brambilla, T. Corti, D. Majus, O. de, and M. Kolesik, "Practitioner's guide to laser pulse propagation models and simulation," European Physical Journal: Special Topics **199**, 5 (2011).

70. J. H. Bechtel and W. L. Smith, "Two-photon absorption in semiconductors with picosecond laser pulses," Phys. Rev. B **13**, 3515 (1976).

71. A. M. Kulibekov, K. Allakhverdiev, D. A. Guseinova, E. Y. Salaev, and O. Baran, "Optical absorption in GaSe under high-density ultrashort laser pulses," Optics Communications **239**, 193 (2004).

72. K.-H. Lee, W.-R. Cho, J.-H. Park, J.-S. Kim, S.-H. Park, and U. Kim, “Measurement of free-carrier nonlinearities in ZnSe based on the Z-scan technique with a nanosecond laser,” Opt. Lett. **19**, 1116(1994).

73. G. N. Patwardhan, J. S. Ginsberg, C. Y. Chen, M. M. Jadidi, and A. L. Gaeta, "Nonlinear refractive index of solids in mid-infrared," Optics Letters **46**, 1824 (2021).

74. W. Li, Y. Li, Y. Xu, J. Lu, P. Wang, J. Du, and Y. Leng, "Measurements of nonlinear refraction in the mid-infrared materials $ZnGeP_2$ and $AgGaS_2$," Applied Physics B: Lasers and Optics **123**, 82 (2017).